AGU PUBLICATIONS

JGR

Journal of Geophysical Research: Earth Surface

RESEARCH ARTICLE
10.1002/2015JF003700

Key Points:
- Spatial variations of snow instability at the basin scale were quantified
- Meteorological processes interacting with terrain caused observed variations
- Snow cover modeling allowed identifying causes of instability variations

Correspondence to:
B. Reuter,
reuter@slf.ch

Citation:
Reuter, B., B. Richter, and J. Schweizer (2016), Snow instability patterns at the scale of a small basin, *J. Geophys. Res. Earth Surf.*, *121*, 257–282, doi:10.1002/2015JF003700.

Received 19 AUG 2015
Accepted 9 DEC 2015
Accepted article online 15 DEC 2015
Published online 12 FEB 2016

Snow instability patterns at the scale of a small basin

Benjamin Reuter[1], Bettina Richter[1], and Jürg Schweizer[1]

[1]WSL Institute for Snow and Avalanche Research SLF, Davos, Switzerland

Abstract Spatial and temporal variations are inherent characteristics of the alpine snow cover. Spatial heterogeneity is supposed to control the avalanche release probability by either hindering extensive crack propagation or facilitating localized failure initiation. Though a link between spatial snow instability variations and meteorological forcing is anticipated, it has not been quantitatively shown yet. We recorded snow penetration resistance profiles with the snow micropenetrometer at an alpine field site during five field campaigns in Eastern Switzerland. For each of about 150 vertical profiles sampled per day a failure initiation criterion and the critical crack length were calculated. For both criteria we analyzed their spatial structure and predicted snow instability in the basin by external drift kriging. The regression models were based on terrain and snow depth data. Slope aspect was the most prominent driver, but significant covariates varied depending on the situation. Residual autocorrelation ranges were shorter than the ones of the terrain suggesting external influences possibly due to meteorological forcing. To explore the causes of the instability patterns we repeated the geostatistical analysis with snow cover model output as covariate data for one case. The observed variations of snow instability were related to variations in slab layer properties which were caused by preferential deposition of precipitation and differences in energy input at the snow surface during the formation period of the slab layers. Our results suggest that 3-D snow cover modeling allows reproducing some of the snow property variations related to snow instability, but in future work all relevant micrometeorological spatial interactions should be considered.

1. Introduction

Predicting snow instability in time and space is hampered by our limited knowledge of the inherently variable nature of the mountain snowpack. Based on point observations or modeling at specific locations, we can typically not conclude on the scale and degree of spatial variations of instability [e.g., *Conway and Abrahamson*, 1988; *Jamieson and Johnston*, 1993]. For reliable spatial prediction one would need to know the drivers of instability as well as their temporal evolution. In other words, a link between the observed variations of snowpack properties and the meteorological drivers, such as precipitation, wind and radiation, and terrain, has to be established. Once the link is established; i.e., we know how meteorological drivers cause variations in snowpack properties and thereby control stability, it will become possible to anticipate stability variations based on the type of meteorological conditions. Of course, extrapolation can be circumvented, if the spatial patterns of snowpack properties could be captured by either (airborne) remote sensing techniques or by modeling the snow cover over 3-D terrain. The latter would certainly be the most elegant approach, provided the model includes a snow instability module so that snow instability patterns can be predicted but requires meteorological input data distributed on a high-resolution terrain model.

Spatial variations, or more generally disorder, are considered to be fundamental for the fracture process [*Anderson*, 2005], and hence, studying spatial variations is to be envisaged in the context of avalanche formation [*Schweizer et al.*, 2008b]. At the slope scale, the scale and degree of spatial variations is supposed to control the avalanche release probability by either facilitating localized failure initiation or hindering extensive crack propagation. However, the role of spatial variations in overall slope instability remained so far purely conceptual and rather hypothetical [*Kronholm and Schweizer*, 2003]—though numerical simulations confirmed some of the anticipated relations between, for instance, the correlation length of snow properties and avalanche size [*Fyffe and Zaiser*, 2004; *Gaume et al.*, 2015; *Kronholm and Birkeland*, 2005]. Variations beyond the slope scale may control the size of slab avalanches by confining their outline since propagating cracks may arrest at distinct discontinuities of the snowpack in particular where terrain properties change.

At the slope scale, most studies aiming at characterizing snow cover variability and studying its causes or its relation to snow instability were first based on arrays of stability tests [e.g., *Campbell and Jamieson*, 2007; *Conway and Abrahamson*, 1984; *Föhn*, 1989; *Jamieson and Johnston*, 1993]. More recently, snow cover data were gathered with the snow micropenetrometer (SMP) allowing a higher sampling rate and terrain coverage than with stability tests. Most studies investigated the spatial variations of layer properties [e.g., *Kronholm et al*., 2004; *Lutz and Birkeland*, 2011], but some also addressed snow instability variations [e.g., *Hendrikx et al*., 2009; *Simenhois and Birkeland*, 2009].

Birkeland et al. [2004a] reported the absence of linear spatial trends of the penetration resistance of buried surface hoar layers on two slopes in Montana. A later geostatistical analysis [*Birkeland et al*., 2004b], however, revealed spatial autocorrelation of weak layer penetration resistance on one slope after log transformation and outlier removal. *Birkeland et al*. [2004b] discussed the challenges involved with spatial snowpack data and with geostatistical data analysis in this field. Although the snow cover can be approximated as a substratum of unique and spatially continuous layers [*Kronholm et al*., 2004], each layer's properties may vary significantly in space. For this reason geostatistical analysis techniques are promising, but they require robust regression techniques [*Papritz et al*., 2013] and the right choice of the sampling design to resolve prevailing snow cover variations, despite safety concerns and time constraints [*Elder et al*., 2009]. Different sampling designs were analyzed by *Kronholm and Birkeland* [2007] who highlighted the need for sufficient resolution and recommended to include some randomness in stratified grids. *Birkeland et al*. [2004b] reported that slab layer properties had an autocorrelation range of a couple of meters but only in a few cases spatial patterns were identified at all in the residuals of the linear trend model. At the slope scale also *Lutz et al*. [2007] analyzed weak layer penetration resistance for two cases and found similar autocorrelation ranges as *Kronholm et al*. [2004] who reported typical values of between 4 and 11 m. In contrast, repeated weekly measurements of weak layer strength using the shear frame on two slopes initially showed weak autocorrelation at very short ranges of about 1 m and was smoothened to a random field after only 2 weeks [*Logan et al*., 2007]. The observed temporal evolution may have been caused by internal processes such as sintering, as external forcing due to variations in terrain properties was absent—as is typically the case at the slope scale.

Kronholm et al. [2004] attributed rather uniform weak layer properties and more variable slab layer properties to calm weather during the weak layer formation period and rather windy conditions thereafter. Relating meteorological parameters to snow properties directly is not straightforward due to the temporal aspect [*Logan et al*., 2007]. Snow layers form during certain weather periods and are subject to metamorphism thereafter. That is why in the past, indicators have been used summarizing the meteorological influence such as the sum of energy fluxes at the snow surface [*Reuter and Schweizer*, 2012] or the variation in wind speed, which was considered a potential measure of turbulence. *Schweizer et al*. [2008a] attempted to relate the variation in penetration resistance of the surface layer to the standard deviation of 10 min maximum wind speed—but found no significant correlation. Also, the role of terrain, vegetation, and micrometeorological characteristics on surface hoar thickness in a forest opening has been studied by *Lutz and Birkeland* [2011]. They reported autocorrelation ranges of several meters for the thickness of surface hoar layers on a slope they sampled repeatedly with the snow micropenetrometer.

Studies investigating the spatial structure of objective measures of snow instability are rare, not least because point snow instability is considered the result of a nontrivial interaction of weak and slab layer properties. *Bellaire and Schweizer* [2011] used a SMP-derived parameter presented by *Bellaire et al*. [2009] and determined an autocorrelation range of several meters in 7 out of 11 field campaigns at the slope scale but could not identify a relation with slope instability. Recently, *Schweizer and Reuter* [2015] reanalyzed the data set of *Bellaire and Schweizer* [2011] and applied a refined snow instability algorithm accounting for slab and weak layer properties yielding a fair correlation with compression test scores. Still, they were not able to relate their point stability results to slope stability despite a geostatistical analysis. *Hendrikx et al*. [2009] assessed clustering of extended column test propagation results as a measure of point snow instability and found that out of four slopes in total two were clustered and two were not. They suggested that the observed clustering into propagation and nonpropagation areas on the slopes may explain weak layer fracturing without subsequent release as reported by *Birkeland et al*. [2006]; cracks may initiate but then arrest in strong areas of the slope.

At the basin scale, contrary to the slope scale, topographic variations are clearly more pronounced and for that reason drivers such as radiation or snow transport by wind cause variations in snow properties

[*Schweizer and Kronholm*, 2007]. *Schirmer et al*. [2011] showed that snow depth variations within a basin were altered by average wind speed and terrain. *Winstral et al*. [2002] successfully reproduced basin scale snow accumulation patterns from a model based on simple terrain parameters. By modeling wind events with flow fields derived from an atmospheric model even small-scale features such as dunes measured with terrestrial laser scans were reproduced [*Mott et al*., 2010]. As such small-scale variations are resolved, their approach promises that given high temporal resolution also snow stratigraphy may spatially be well resolved. So it may be possible to identify meteorological causes for spatial variations of stratigraphy—or even instability.

So far, however, only a small number of studies have addressed the causes of snow instability variations. At the scale of a mountain range, *Birkeland* [2001] suggested that aspect and elevation may serve as predictors of snow instability. *Schweizer et al*. [2003b] also related stability to terrain while analyzing stability patterns at the regional scale; however, on different sampling days different patterns with regard to aspect and elevation were observed. They found increasing point stability with increasing snow depth and identified the primary weakness to be due to a cold period causing faceting around crusts within the snowpack. Relating objective measures of snow instability to aspect, slope angle, and snow depth, *Reuter et al*. [2015b] partly explained snow instability variations in a nonspatial analysis with different combinations of these parameters. These findings may provide guidance for investigating causes of instability and, in general, help to enhance instability predictions.

Two approaches can be generally thought of in order to obtain the spatial structure of snow instability, interpolation of the target variable from point measurements of the target variable, or modeling of the target variable on gridded, possibly interpolated explanatory data.

The first approach, which is based on field measurements, was hampered in the past by inadequate measures of snow instability and/or small sample sizes not amenable to geostatistical analysis [e.g., *Bellaire and Schweizer*, 2011; *Campbell and Jamieson*, 2007]. With developments in field measurement techniques, however, snow properties can be measured independent of observer [*Schneebeli et al*., 1999] and with good accuracy [*Proksch et al*., 2015]. These developments allowed the first geostatistical analyses of snow layer properties such as penetration resistance [e.g., *Kronholm et al*., 2004]. Concurrently, SMP-derived metrics such as the microstructural compressive strength [*Johnson and Schneebeli*, 1999] were related to stability test results [*Bellaire et al*., 2009; *Pielmeier and Marshall*, 2009; *Pielmeier and Schweizer*, 2007]. More recently, two criteria of instability were suggested that relate to the two key processes in dry-snow slab avalanche release (failure initiation and crack propagation); the two metrics were clearly related to independent observations of instability [*Reuter et al*., 2015a].

To interpolate field measurements, geostatistical methods were preferred over simple regression techniques to interpolate observations of snow properties or snow instability. One reason for the preference is that snow instability observations are time consuming which limits exhaustive sampling to achieve densely spaced observations that would allow simple interpolation. Also, experience suggests that patterns of snow instability exist, and hence, methods to obtain measures of autocorrelation were chosen [*Kronholm*, 2004]. In order to describe the spatial distribution of weak layer properties, maps of weak layer penetration resistance were presented and qualitatively related to arrays of point stability observations [*Schweizer et al*., 2008b]. *Bellaire* [2010] described the spatial autocorrelation based on topographic coordinates and interpolated weak layer strength by ordinary kriging. Based on his data, the first maps of snow instability were presented by *Schweizer and Reuter* [2015] who introduced a simple index of instability considering the mechanical interplay of the weak layer and the slab.

Geostatistical modeling approaches taking into account so called covariate information, i.e., additional information indicative of the quantity to be predicted and available on the entire interpolation grid, were applied to snow depth distributions by *Gaume et al*. [2013]. They presented spatial interpolations of annual maxima of the 3 day sum of precipitation based on climate regions and elevations as covariates in the French Alps. In order to interpolate surface air temperatures over Switzerland, *Frei* [2014] divided surface air temperature variations into meteorological meaningful "background" and "residual" patterns and eventually performed spatial interpolations by weighting residuals for topographic effects. In complex terrain the spatial interpolation of meteorological parameters may profit from correlations with any kind of environmental parameters so that kriging techniques are widely used in meteorological applications

[e.g., *Perčec Tadić*, 2010]. Hence, including covariate information for spatial interpolation currently seems the most appropriate approach in cases of different scale processes being superimposed in complex terrain.

With regard to the second approach, modeling snow layer properties from gridded meteorological data in space and time builds upon modeling of snow stratigraphy in one vertical dimension and preferably includes spatial interactions such as preferential deposition and redistribution of snow or radiative processes [*Lehning et al*., 2006]. Meanwhile, models simulating the surface radiation balance in complex terrain are available, and their performance under clear and overcast skies was validated with measured radiation components yielding good agreements [*Helbig et al*., 2010]. Also, snow accumulation features were reproduced by snow transport models [*Vionnet et al*., 2014], even resolving small-scale features such as dunes, if a sufficient resolution (5 m) was chosen [*Mott et al*., 2010].

Once the spatial structure of snow stratigraphy is obtained, these data can be used as input into mechanical models that take into account the spatial interactions between gridded point instability data in order to simulate snow slope instability and eventually predict avalanche release. For instance, *Gaume et al*. [2014] applied stochastic-finite element simulations to model slope instability from weak layer heterogeneity. They demonstrated a knock-down effect on slope instability depending among others on the coefficient of variation of weak layer cohesion. The influence of the coefficient of variation of weak layer shear strength was earlier described by *Fyffe and Zaiser* [2004], who used a cellular automaton model for the investigation of snow slope instability. *Kronholm and Birkeland* [2005] used measured shear strength distributions for their cellular automaton model with modifications regarding the distributions of initial shear strength values to investigate the size of the fractured area. By keeping snowpack parameters constant, but varying the spatial structure, they obtained results indicating that large-scale spatial structures favor crack propagation. They noted that field measurements confirming the hypothesis are still lacking.

Basin scale snow instability variations have rarely been studied and their causes are largely unknown. By applying advanced geostatistical methods to objective metrics of snow instability, we aim at identifying spatial patterns of snow instability and their drivers at the basin scale. We analyze a field data set consisting of five campaigns comprising data on snow depth, terrain, and snow properties mainly acquired with the snow micropenetrometer in a small basin above tree line. From our field measurements we modeled the autocorrelation structure of snow instability using snow depth and terrain data as covariates. In order to identify patterns of snow instability we performed external drift kriging and mapped the variations of instability. Furthermore, we used modeled snow properties as covariates and repeated the geostatistical analysis. This approach, using snow cover model output, is an initial attempt to explore the causes of the observed patterns of instability by tracking how meteorological conditions shaped the snow layer properties.

2. Methods

In the following sections we describe the field data collection, explain the SMP signal processing, introduce the two snow instability criteria used, and provide a detailed description of the geostatistical methods for spatial interpolation. With regard to the field data, essentially the same data have been analyzed nonspatially by *Reuter et al*. [2015b].

2.1. Field Data

Throughout the winter seasons between 2010 and 2013 we sampled the Steintälli basin above Davos (Eastern Swiss Alps; 46.81°N, 9.79°E) 13 times but only for five of the field campaigns we acquired a complete data set. Measurements were performed at 150 locations according to a sampling design spanning about 400 m × 400 m presented in Figure 1. Our field records contain profiles of snow penetration resistance measured with the snow micropenetrometer, locations measured with differential GPS, manual measurements of aspect, snow depth and slope angle, terrestrial laser scans, manual snow profiles, and snow instability observations. The sampling design consists of 25 partly randomized cell arrays allowing for subsequent measurements and easy orientation during data collection in the field while sampling most diverse distance pairs, called lag distances in the geostatistical context. The distribution of lag distances is presented in the histogram of Figure 2. For distances between 10 m and 380 m at least 100 lag pairs are available per bin given a bin width of 10 m. Hence, the selected design provides a reasonably dense coverage for studying local differences of snow properties at the basin scale. With regard to the scale triplet [*Blöschl and Sivapalan*, 1995],

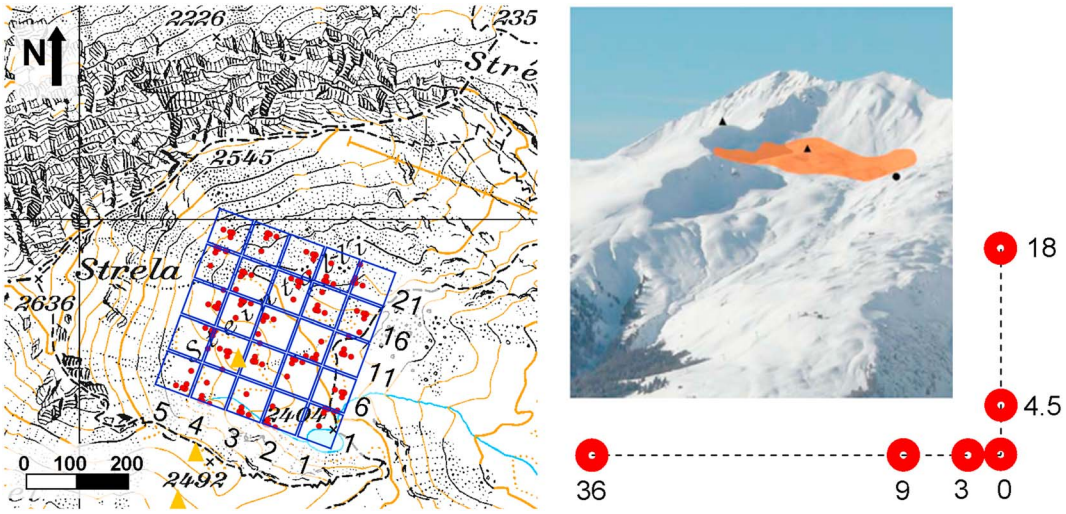

Figure 1. (left) Map of field site showing all 25 cells (blues boxes with numbering along the sides) each with L-shaped sampling array (red points) including six SMP measurements and measurements of terrain parameters and snow depth. Manual snow profiles were conducted at corner points of the "L" in cells 1, 5, 7, 9, 13, 17, 19, 21, and 25, GPS measurements in all cells at corner points. Contour line interval is 20 m and cell size is 80 m. (top right) View of the field site below the Strela summit (orange overlay) from the SE. Laser scan location by black dot and weather stations by black triangles. (bottom right) L-shaped sampling design illustrated; distances from corner point in meters.

the support was on the order of 10^{-5} m^2, corresponding to the area of the SMP tip, the minimum spacing 3 m, and the maximum extent was about 500 m.

To obtain accurate measurement locations, we performed differential GPS measurements yielding coordinates with submeter accuracy at the corner points. The other sampling locations in a grid cell were then determined with a measuring tape and compass northing. Further terrain parameters including slope angle and aspect were measured manually. Snow depth was measured with a probe at every measurement location but is also available from a terrestrial laser scan.

During all field campaigns a terrestrial laser scan (TLS) was performed from an exposed location overlooking the Steintälli (Figure 1). We used the Riegl LPM-321 device operating at 905 nm [*Veitinger et al.*, 2014]. The suitability of this device was demonstrated by *Prokop* [2008] and *Prokop et al.* [2008]. Its accuracy was determined by *Grünewald et al.* [2010] in comparisons with Tachymeter measurements at distances up to 250 m (mean deviation of 4 cm and standard deviation of 5 cm). In order to minimize vibration effects due to wind and keep errors due to settling and tilting small, the device was installed on a tripod on solid rock.

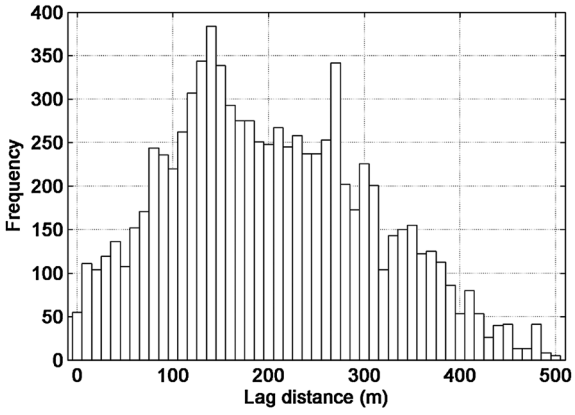

Figure 2. Histogram of lag distances of measurements performed on the 3 March 2011.

To facilitate georeferencing of the scans, we had used reflecting plates installed in rock walls or attached to weather stations at different distances and angles from the measurement location. Eventually, the spatial distribution of snow depth was calculated by subtracting a digital terrain model obtained with the TLS sampling technique as well. The resulting snow depth data have a resolution of 1 m. However, due to terrain shading in grid cells 1 to 5 (Figure 1) some areas are not covered.

Concurrent snow instability observations included nine snow profiles in grid cells 1, 5, 7, 9, 13, 17, 19, 21, and 25 as well as stability tests and observations of signs of instability. The snow profiles were performed

following the International Classification for Seasonal Snow on the Ground (ICSSG) guidelines [*Fierz et al*., 2009] and contain information on snow layering, grain type and size, and hand hardness index. An exemplary snow profile representing the characteristic snowpack layering for each sampling day is provided in the Appendix (Figure A1). We performed propagation saw tests [*Gauthier and Jamieson*, 2008], extended column tests [*Simenhois and Birkeland*, 2009], and compression tests [*Jamieson and Johnston*, 1997]. Signs of instability [e.g., *Haladuick et al*., 2014; *Jamieson et al*., 2009] were recorded with time and location.

The avalanche danger forecast was verified based on our snow instability observations in the field [*Schweizer et al*., 2003b] and is described according to the European avalanche danger scale increasing from low (1), moderate (2), considerable (3), high (4), to very high (5) [*Meister*, 1995].

2.2. Snow Micropenetrometer Signal Analysis

The snow micropenetrometer (SMP) is a constant speed penetrometer which records microstructural and mechanical snow profile information. The signal we obtain from an SMP measurement is a depth-resistance record. Due to the high measuring frequency of about 250 samples per millimeter and a constant penetration speed of 20 mm s^{-1}, the penetration resistance signal may be interpreted as a Poisson shot noise process, which recovers the following properties from the signal: rupture force, deflection at rupture, and structural element size [*Löwe and van Herwijnen*, 2012]. After 2.5 mm moving window averaging and an overlap of 50% the effective resolution is eventually 1.25 mm. In order to reduce computation times we introduced layers and assigned mean values obtained from the moving window averaging. The layering was consistent at the field site, and hence, we selected the same slab layers and the same weak layer, according to the most prominent weakness found in stability tests and manual snow profiles. The layer properties included snow density ρ derived following *Proksch et al*. [2015], the weak layer fracture energy w_f calculated according to *Reuter et al*. [2015a], and the effective modulus E and the strength σ as described by *Johnson and Schneebeli* [1999].

Thus, at every SMP measurement location, snow stratigraphy was characterized by the relevant mechanical properties: ρ and E for the slab layers, w_f and σ_{WL} for the weak layer, and ρ and E for the basal layers. Following the recently presented approach by *Reuter et al*. [2015a], the failure initiation criterion S and the critical crack length r_c were derived as estimates of snow instability.

2.3. Snow Instability Criteria

A criterion S describing the likelihood of initiating a failure at the depth of the weak layer was defined by *Reuter et al*. [2015a] as

$$S = \frac{\sigma_{WL}}{\Delta\tau}\ , \tag{1}$$

where σ_{WL} is the strength of the weak layer and $\Delta\tau$ the maximum shear stress within the weak layer due to skier loading only. The maximum shear stress under the stratified slab was obtained with a linear elastic finite element simulation.

The critical crack length r_c for unstable crack propagation is regarded as a criterion for the snowpack's propensity to support crack propagation in a weak layer [e.g., *Sigrist and Schweizer*, 2007]. The critical crack length was obtained as the solution of an analytical beam equation for a uniform slab. The stratigraphic properties of the slab were accounted for by deriving the bulk effective modulus from a finite element simulation of the stratified slab, as assuming a uniform slab yields unrealistic estimates of the mechanical deformation energy [*Reuter et al*., 2015a].

2.4. Covariates for Statistical Modeling

To improve predictions between sampling locations, we used slope aspect, slope angle, snow depth, and elevation which have been confirmed to be potential drivers of snow instability at the basin scale [*Reuter et al*., 2015b]. These potential drivers will be used as covariates of our trend models (see below) as they have a physical relationship with the response variables, our two snow instability metrics, we attempt to model. Slope aspect, slope angle, and elevation were available from a 1 m resolution digital elevation model covering the Steintälli field site. The elevations of field measurement locations were determined with measured coordinates from the locations in the DEM, whereas for slope aspect and slope angle the manual measurements were used. Snow depth data were available from manual measurements at every

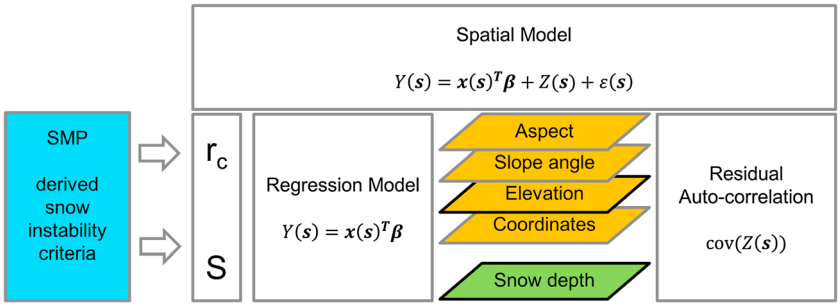

Figure 3. Flowchart presenting the workflow followed within the geostatistical analysis to model the spatial structure of snow instability. From SMP-derived snow properties (blue box) the snow instability criteria (S and r_c) were derived. The regression model is built on the significant covariates (elevation and snow depth, for instance) selected from the four covariates available from DEM (orange boxes) or TLS data (green box). The spatial structure was modeled as a linear regression model and a residual autocorrelation.

measurement location and repeated laser scans of the Steintälli field site [*Veitinger et al.*, 2014]. Due to its circular nature, slope aspect (0–360°) is not amenable to statistical analysis and was hence decomposed into four periodic B splines for each aspect category, thus peaking at the distinct aspects (E, N, W, and S) and reaching zero at their opponent aspect (W, S, E, and N). If aspect was a significant covariate, only two nonopponent B splines were included as the B spline of the opponent aspect is redundant each.

2.5. Geostatistical Analyses

2.5.1. Spatial Autocorrelation

Exploring an underlying spatially continuous phenomenon in a finite sample of measured values and predicting for unsampled locations based on the identified spatial structure is the core aim of geostatistical techniques [*Webster and Oliver*, 2007]. With regard to snow instability at the basin scale, we are first interested in the prediction of values of snow instability at locations we did not sample in order to map snow instability in an alpine basin. Second, an analysis of prediction errors is required to assess the uncertainty involved with the mapping but also to compare predictions based on two types of covariate data: terrain and snow depth information from a digital elevation model (DEM) and from terrestrial laser scans (TLS) on one hand and snow cover model output on the other.

For the prediction of the two instability metrics over our study area we will develop a geostatistical (or spatial) model Y that divides the instability variations into a physical meaningful background (based on the above mentioned covariates) and residual patterns and then perform spatial interpolations based on the background field and residual patterns [*Frei*, 2014; *Nussbaum et al.*, 2014]. The background field (describing the external drift) was modeled as a linear regression model, whereas the residual field, the second part describing the autocorrelation, was modeled as a stationary autocorrelated Gaussian random field. The workflow we followed is presented in Figure 3.

The background field, represented by a linear external drift model, is determined by processes varying smoothly with topographic features, such as solar radiation depending on slope angle and aspect, leading to rather large-scale patterns. Smaller scale variations imprinted on the background field, for instance, snow accumulation patterns caused by wind, e.g., dunes, may be captured by the residual autocorrelation.

The response variables were the SMP-derived failure initiation criterion S and the critical crack length r_c. Covariate data available for the area of the sampling domain consisted of DEM data, providing aspect, slope angle, elevation, and the topographic coordinates, and TLS data providing the current snow depth at the time of our field campaigns. For the geostatistical analysis only significant covariates were selected.

Snow instability was derived from SMP measurements at locations $\boldsymbol{s} = (s_1, s_2)$ giving an array of observed values $\boldsymbol{y(s)}$ for each of both instability criteria S and r_c. Covariate information $\boldsymbol{x}(\boldsymbol{s})$ was collected at the locations of the SMP measurements in the field. Hence, $\boldsymbol{y}$ and $\boldsymbol{s}$ have length n and $\boldsymbol{x}$ has size (n, p), with n being the number of observations and p the number of covariate variables.

The spatial model $Y(\boldsymbol{s})$ that describes the variations in our observations at the field measurement locations $\boldsymbol{s}$ has the following form:

$$Y(\boldsymbol{s}) = \boldsymbol{x}(\boldsymbol{s})^{\boldsymbol{T}}\boldsymbol{\beta} + Z(\boldsymbol{s}) + \varepsilon(\boldsymbol{s}), \tag{2}$$

where $\boldsymbol{x}(\boldsymbol{s})^{\boldsymbol{T}}\boldsymbol{\beta}$ describes the external drift with coefficients $\boldsymbol{\beta}$, $Z(\boldsymbol{s})$ is a spatially stationary autocorrelated Gaussian process with zero mean and covariance cov (Z), and uncorrelated fluctuations $\varepsilon(\boldsymbol{s})$ with zero mean, i.e., independently distributed errors.

As our data set does not contain a large number of replicated measurements at the same locations, we cannot separate measurement errors and sub grid fluctuations. Hence, we ignore $\varepsilon(\boldsymbol{s})$ and all fluctuations from the autocorrelated variation are summarized in the "nugget" variance τ^2; hence, the covariance of Z can be given as

$$\mathrm{cov}(Z) = \sigma^2\boldsymbol{V}_{\rho} + \tau^2\boldsymbol{I}, \tag{3}$$

with $\boldsymbol{V}_{\rho}$ being the correlation matrix and $\boldsymbol{I}$ the identity matrix, σ^2 is the variance of the autocorrelated variation (also called the sill variance) in Z, and τ^2 the nugget variance of $Z(\boldsymbol{s})$ that cannot be resolved with the chosen sampling design plus measurement errors.

To select significant covariates, we performed stepwise multiple linear regressions between the response variables $\boldsymbol{y}$ and the covariates $\boldsymbol{x}$ and provide the adjusted coefficient of determination ${R_a}^2$. The quality of the external drift model was assessed by residual diagnostics to ensure the spatial stationarity assumption is fulfilled [*Diggle and Ribeiro*, 2007]. In case residuals showed nonstationary behavior (i.e., considerable drift with increasing fitted values) the response was log transformed for the spatial autocorrelation analysis and eventually back transformed for the spatial prediction. Based on their correlation, we assured that redundant covariates were excluded. With the Akaike information criterion we ensure that model improvement by including additional covariates is exhausted [*Draper and Smith*, 1998].

Whereas it is common practice to derive the autocorrelation structure from the experimental variogram that relates the residuals of an external drift model to the lag distances [*Webster and Oliver*, 2007], this approach is not well suited for data including significant outliers. As in our field data records outlying observations are not rare, they will affect estimates of the external drift model and the autocorrelation parameters. Methods less sensitive to outliers are therefore preferred to obtain robust statistical estimates. *Papritz et al*. [2013] presented a robust approach for identifying the autocorrelation structure of a Gaussian random field which has been applied by *Nussbaum et al*. [2014] to soil data. We followed their procedure to obtain robust estimates of the covariance parameters of the variogram $\boldsymbol{V}$ of the residuals of our external drift model, with lag distances $\boldsymbol{u}$, nugget variance (τ^2) summarizing fluctuations and measurement errors, signal variance (σ^2) of the autocorrelation, and correlation function ρ_a; the latter includes the range r_a:

$$\boldsymbol{V}(\boldsymbol{u}) = \frac{1}{2}\mathrm{var}(Z(\boldsymbol{s}) - Z(\boldsymbol{s}-\boldsymbol{u})) = \sigma^2(1-\rho_a(\boldsymbol{u})) + \tau^2. \tag{4}$$

The most likely variogram parameters fitting the variogram $\boldsymbol{V}$ can be determined by optimizing the log likelihood function $L(\boldsymbol{y}; \sigma^2, \tau^2, r_a, \boldsymbol{\beta})$ relating the model parameters with their joint probability of the multivariate distribution $f(\boldsymbol{y}; \sigma^2, \tau^2, r_a, \boldsymbol{\beta})$. Under the assumption of $\boldsymbol{y}$ being Gaussian with a linear trend the joint probability density function $f(\boldsymbol{y}; \sigma^2, \tau^2, r_a, \boldsymbol{\beta})$ is explicit,

$$L = -\frac{1}{2}\left[\ln(2\pi) + \ln\left(\det\left(\sigma^2\boldsymbol{V}_{\boldsymbol{a}}(r_a) + \tau^2\boldsymbol{I}\right)\right) + \left(\boldsymbol{y} - \boldsymbol{x}^{\boldsymbol{T}}\boldsymbol{\beta}\right)^T\left(\sigma^2\boldsymbol{V}_{\boldsymbol{a}}(r_a) + \tau^2\boldsymbol{I}\right)^{-1}\left(\boldsymbol{y} - \boldsymbol{x}^{\boldsymbol{T}}\boldsymbol{\beta}\right)\right]. \tag{5}$$

Maximizing this equation yields a system of equations for the regression coefficients and the covariance parameters. By generalized least squares estimation both the regression coefficients $\boldsymbol{\beta}$ and the covariance parameters (σ^2, τ^2, and r_a) are obtained [*Papritz*, 2013]. In addition, resampled partitions of the data were also used to optimize the profile likelihood function (restricted maximum likelihood estimation) to reduce the nuisance in small samples as ours. In our case the equivalent number of independent observations (49) is about less than one third of the nominal sample size (~150). By taking into account the autocorrelation of 11,175 variogram sample pairs from only 150 different sampling locations the maximum likelihood estimation approach brings a large benefit as it yields less biased variance estimators compared to ordinary least squares fitting techniques.

We obviously do not know the spatial structure of snow instability, i.e., whether snow instability has a rough or rather smooth surface representation in the terrain. To not limit ourselves to a specific correlation function, we selected the most appropriate one from the Matérn "family" of correlation functions [*Diggle and Ribeiro*, 2007]. The shape parameter η varied $\eta = [0.5, 1.5, 2.5]$; a value of $\eta = 0.5$ corresponds to the exponential variogram representing a rather rough surface, whereas the higher values of the shape parameter yield two smoother fitting models being once ($\eta = 1.5$) or twice differentiable ($\eta = 2.5$). The choice between the models was taken based on the maximized restricted log likelihood. Apart from different surface roughness models, staying within the Matérn family allows comparisons of the covariance parameters such as the resulting autocorrelation range. The computation was carried out in R [*R Core Team*, 2013].

2.5.2. Spatial Prediction

In order to map snow instability variations within the Steintälli, we use the spatial model described above including the autocorrelation structure and perform external drift kriging to obtain predictions of snow instability [*Papritz*, 2013].

The predicted surface $\hat{\boldsymbol{Y}}$ is generated for all locations $\boldsymbol{s_0}$, also those without observations, by combining the underlying external drift model with the estimated coefficients $\hat{\boldsymbol{\beta}}$ and the estimated covariance structure of the data:

$$\hat{\boldsymbol{Y}}(\boldsymbol{s}_0) = \boldsymbol{x}(\boldsymbol{s}_0)^T \hat{\boldsymbol{\beta}} + \gamma_a(\boldsymbol{s} - \boldsymbol{s}_0)^T (\mathrm{cov}_a(Z(\boldsymbol{s})))^{-1} \hat{Z}(\boldsymbol{s}), \tag{6}$$

where the second term on the right contains a vector γ of estimated covariance between $Z(\boldsymbol{s})$ and $Z(\boldsymbol{s_0})$, the estimated covariance matrix of the Gaussian process at sampled locations $Z(\boldsymbol{s})$, and the vector with the kriging predictions (estimated residuals $\hat{Z}$) of sampled locations $\hat{Z}(\boldsymbol{s})$. The superscript "hat" indicates that values from the restricted maximum likelihood algorithm are used and the subscript "*a*" indicates that the covariance parameters enter the estimation of the function. Thus, the prediction compromises between the external drift, i.e., the background field, and the autocorrelation structure observed in the measurement data. In other words, it depends on the properties of the target location $\boldsymbol{x}(\boldsymbol{s_0})$, i.e., the covariates at the target location, but also on the sampling locations $\boldsymbol{s}$, i.e., the sampling design, and on the identified covariance structure, i.e., the covariance model parameters summarized by the subscript *a* (autocorrelation structure). Thus, the background field gives a first estimation and then the interpolation is refined with the autocorrelation structure; in other words, we add estimates of the fluctuations we obtained from the analysis of the residual patterns.

As the parameters we chose as covariates partly explain the snow instability variations, they may enhance the prediction at locations we did not sample by introducing local differences which would be missed by ordinary regression lacking covariate information. If, however, the geostatistical analysis does not reveal a spatial dependence, the external drift kriging would simply reduce to a multiple linear regression of the drift model $\boldsymbol{x}^T \hat{\boldsymbol{\beta}}$.

The quality of the predictions is assessed by comparing the predictions at the locations where the measurements were performed with the tenfold cross validation approach. After separating the observed data into 10 random samples, the model is refitted from 9 out of 10 samples and compared to the omitted tenth of the observations. Repeating the procedure 10 times gives an estimate of the prediction accuracy.

2.6. Snow Cover Modeling and Identification of Meteorological Drivers

The model system Alpine3D [*Lehning et al*., 2006] was used to model the snow cover and its properties in the Steintälli basin based on the micrometeorological conditions. To this end, a digital elevation and a land cover model, both at a resolution of 4 m in the horizontal, were used [*Bühler et al*., 2012]. Therefore, the meteorological input data are interpolated on the digital elevation and land cover models yielding a 4 m resolution. The Alpine3D model system provides three modules which include the interaction of micrometeorological processes. The modules are related to preferential deposition and redistribution of snow (snow transport), to the energy balance (radiation module), and to internal processes in the snow cover (SNOWPACK). The first two spatially interacting processes (snow transport and radiation) must be included, if spatial variations in snow properties are expected to be simulated. In the following, we refer to the data sources and the model setup in detail.

The model system was driven with data from four automatic weather stations (AWS) located within and around the Steintälli study site between 2440 and 2492 m above sea level (see Figure 1) and at the

Weissfluhjoch study plot (2540 m, 3 km to the northeast of Steintälli) (not shown in Figure 1). Meteorological input contained air temperature and relative humidity (Rotronic MP100H HygroClip, ventilated), wind speed, and direction (YOUNG wind monitor and Lambrecht combined wind sensor 14512), incoming shortwave and longwave radiations (Campbell CNR1), and precipitation (Lambrecht Joss-Tongini). The meteorological input data were interpolated on a grid with size 600 m × 600 m covering the area of field measurements at a resolution of 4 m (module MeteoI/O) [*Bavay and Egger*, 2014]. In case data gaps longer than 1 day existed the data of the AWS were excluded in that particular period. Data gaps shorter than 1 day were filled by linear interpolation. Variables were filtered by introducing reasonable lower and upper limits, e.g., 5 and 100% for relative humidity. Air temperature was interpolated with an elevation lapse rate of 8 K/1000 m and by inverse distance weighting. From air temperature and relative humidity the dew point temperature was calculated, interpolated over the grid by inverse distance weighting, and retransformed into relative humidity. Wind speed was distributed over the grid by applying an elevation lapse rate based on all AWS data and performing inverse distance weighting. Furthermore, the wind speed was corrected at grid points for sheltering of the slope from the wind direction based on aspect, slope angle, and exposure (terrain curvature) [*Liston and Elder*, 2006]. After correcting for undercatch [*Schmucki et al*., 2014] precipitation values were distributed over the grid by inverse distance weighting and including a constant elevation lapse rate. To include wind induced effects during snowfalls a correction for precipitation based on terrain and average wind direction was applied over the grid [*Winstral et al*., 2002].

Spatial variations of micrometeorological processes are also caused by radiation differences. Measurement values from the reference AWS located within the Steintälli (grid cell 9 in Figure 1) provided incoming short and longwave radiation. Shortwave radiation was split into diffuse and direct radiation [*Erbs et al*., 1982]. The contribution of direct shortwave radiation on every grid point was calculated including shading effects based on the DEM. Adding the diffuse part, which is assumed constant over the modeling domain, and accounting for additional terrain reflections by introducing a terrain view factor and the albedo of the reflecting terrain amount to the complete shortwave radiation received at a grid point. Longwave radiation values from all AWS were averaged after correction with a constant elevation lapse rate (-0.031 W $(m^2\ m)^{-1}$) [*Marty et al*., 2002].

Snow properties were modeled by the snow cover model SNOWPACK running within the model framework of Alpine3D. The modeling time step was 60 min after resampling the data from the AWS with a sampling rate of either 10 min or 30 min. The model was initiated on 24 September the year before, when no snow was present at the AWS and ran until the day of the field measurement campaign. Neumann boundary conditions for estimating the snow surface temperature and atmospheric stability corrections for estimating turbulent exchange were the preferred adjustments concerning the energy balance model [*Stössel et al*., 2010].

The snow properties obtained from snow cover modeling include the weak layer shear strength [*Jamieson and Johnston*, 2001], the shear stress at the depth of the weak layer, the load of the slab, the average density of the slab, the slab thickness, and the skier stability index [*Jamieson and Johnston*, 1998]. A principle component analysis was performed on these snow properties to evaluate whether they are suited as covariates for the snow instability criteria obtained from snow micropenetrometer field measurements—for 3 March 2011 when simulated snow properties were available. Then, the geostatistical analysis from above was carried out on the first principle components, including regression model development, determination of covariance parameters, and modeling error estimation by cross validation. The cross-validation errors provide information on the predictive power of the spatial model including covariates as obtained from the snow cover model. In case a similar quality of prediction as with terrain and snow depth data is achieved, snow cover properties may be used interchangeably with terrain parameters.

Snow cover model data have the advantage that they implicitly contain the records of meteorological data of the season. Hence, basing the geostatistical model on covariates from the snow cover model output will enable us to search the meteorological records for the significant meteorological driving agents—i.e., causes of variations. Because in our model setup differences due to spatial interactions are only created by variations in snow transport and radiation, we only selected snow cover properties of the Alpine3D output that were linked to either snow transport or radiation. These properties include the precipitation mass and modeled wind speed, the energy input at the snow surface, and the snowpack's internal energy change. The variables were averaged over the weak or slab layer formation period depending on whether they refer to a weak or a slab layer property. A simple correlation analysis facilitated the search for significant drivers. We report the

Table 1. Regression and Covariance Fitting Models for All Five Field Campaigns and the Two Response Variables S and r_c[a]

	Criterion	Significant Covariates	Log	R_a^2	Matérn η	Range	Likelihood
28 Jan 2011	S	Snow depth + elevation + aspect	Yes	0.45	2.5	31 m	−71
28 Jan 2011	r_c	Coordinates + slope angle + elevation + aspect	No	0.19	2.5	68 m	+98
3 Mar 2011	S	Coordinates + snow depth + slope angle + aspect	Yes	0.30	2.5	5 m	−89
3 Mar 2011	r_c	Snow depth + slope angle + aspect	No	0.13	2.5	7 m	+92
13 Feb 2012	S	Coordinates + snow depth + slope angle + elevation + aspect	Yes	0.56	0.5	15 m	−102
13 Feb 2012	r_c	Coordinates + slope angle + elevation + aspect	Yes	0.45	0.5	10 m	−6
9 Mar 2012	S	Coordinates + snow depth + elevation + aspect	Yes	0.51	0.5	26 m	−89
9 Mar 2012	r_c	Coordinates + elevation + aspect	No	0.33	0.5	7 m	−20
10 Jan 2013	S	Snow depth + slope angle + elevation + aspect	Yes	0.44	0.5	10 m	−94
10 Jan 2013	r_c	Coordinates + slope angle + aspect	No	0.12	0.5	26 m	+155

[a]Furthermore, the information whether the response variable was log transformed (yes/no), the adjusted coefficient of determination (R_a^2) of the regression model, the shape parameter of the Matérn model, the range estimated from the covariance model, and the restricted log likelihood are given.

coefficient of determination (R^2) as a measure of correlation and variance, which is the square of the correlation coefficient in the case of linear correlation.

3. Results

In the following we present the model results for the external drift model, the spatial autocorrelation of the snow instability parameters, and the spatial predictions of the two snow instability metrics for the Steintälli basin. Finally, we report the meteorological variables identified as drivers of snow instability variations for 3 March 2011.

3.1. External Drift Model

First, we developed multiple linear regression models for both instability criteria and all five field campaigns considering the five variables: topographic coordinates, snow depth, slope angle, elevation, and aspect. Table 1 gives an overview on the different regression models. The most important terrain-related driving agent was aspect, which was included in the regression models in all cases. However, the regression models, in general, differed; they contained the coordinates, the slope angle, and the elevation as significant covariates in seven cases, whereas the snow depth entered the regression model in six cases. In most cases a similar set of covariates described the background field of the two instability criteria on a single day. Hence, the agents varied depending on the situation which is in line with the findings of *Reuter et al*. [2015b]. For instance, on 3 March 2011 a quite well settled slab sat on top of a 4 day old weak layer of facets partly grown to depth hoar crystals, whereas on 13 February 2012 a thinner, poorly bonded slab covered smaller, 19 day old faceted crystals. Meteorological processes altered by terrain had caused different vertical snowpack structures in both situations which are then reflected in different sets of driving agents.

In all cases the adjusted coefficient of determination R_a^2 was higher for the failure initiation criterion than for the critical crack length. This indicates that the external drift model better explained the spatial variability in case of the failure initiation criterion. It is not surprising that not all the variance observed in a basin can be explained by a linear regression model. Even though the values of R_a^2 for the regression analysis are modest, a spatial structure may still exist, which eventually will yield good predictions.

3.2. Spatial Autocorrelation

The residuals of the multiple linear regressions showed in all cases spatial autocorrelation even though not as distinct in some cases according to the restricted log likelihood (Table 1 and Figures 4 and 5). The covariance models fitting the variograms best were either the exponential model (equal to Matérn with $\eta = 0.5$) representing a rough surface or the twice differentiable Matérn model with $\eta = 2.5$, representing a smooth surface. With the chosen sampling design autocorrelation ranges between 3 and 250 m can be resolved, where the minimum is the shortest lag pair and the maximum is approximated as half of the maximum extent. On 28 January 2011 the autocorrelation ranges were rather large with 31 m for S and 68 m for r_c compared to 3 March 2011 when 5 m and 7 m were modeled. On both days the small-scale fluctuations (i.e., the nugget variance), which

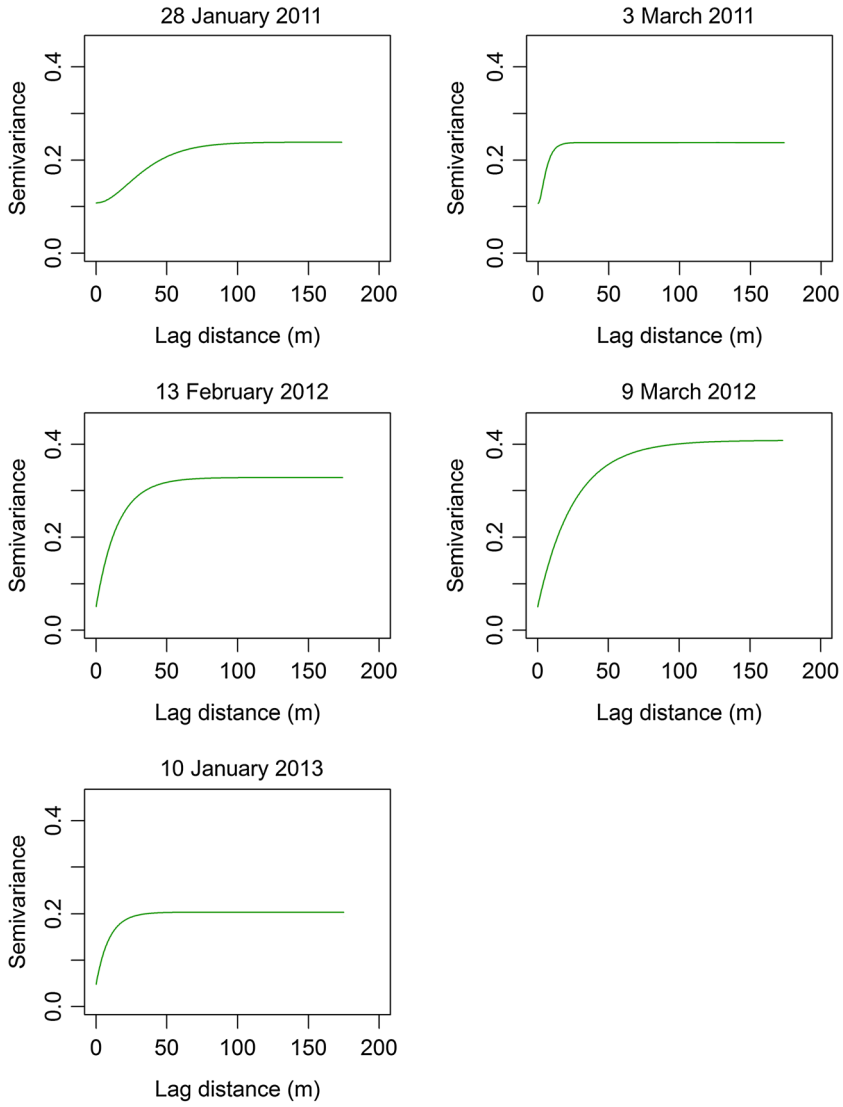

Figure 4. Covariance models of the modeled failure initiation criterion for all five field campaigns estimated with the restricted maximum likelihood method.

summarize measurement errors plus subgrid scale fluctuations, were modeled as smooth surfaces. On the remaining days, namely, 13 February 2012, 9 March 2012, and 10 January 2013, the autocorrelation ranges varied between 7 m and 26 m and the best fitting covariance function was the exponential model. Hence, on these three days, stronger small-scale fluctuations were superimposed on the autocorrelation ranges of both instability criteria, as both snow instability criteria were modeled as rough surfaces. Assuming the measurement error was the same on all days, we can conclude that subgrid scale fluctuations were stronger on these days than on 28 January and 3 March 2011.

In all cases autocorrelation models fitted the residuals of the crack length better than the failure initiation criterion which is reflected in higher values of the restricted log likelihood (Table 1). A large amount of variation of the failure initiation criterion was already explained by terrain and snow depth variations, corresponding to higher R_a^2 for the external drift model of the failure initiation criterion. In the case of the critical crack length, less variation was captured by the external drift model, but the covariance models performed better than for the failure initiation criterion, corresponding to higher values of the restricted log likelihood. Hence, the remaining residual variation was partly captured in the second step when modeling the autocorrelation.

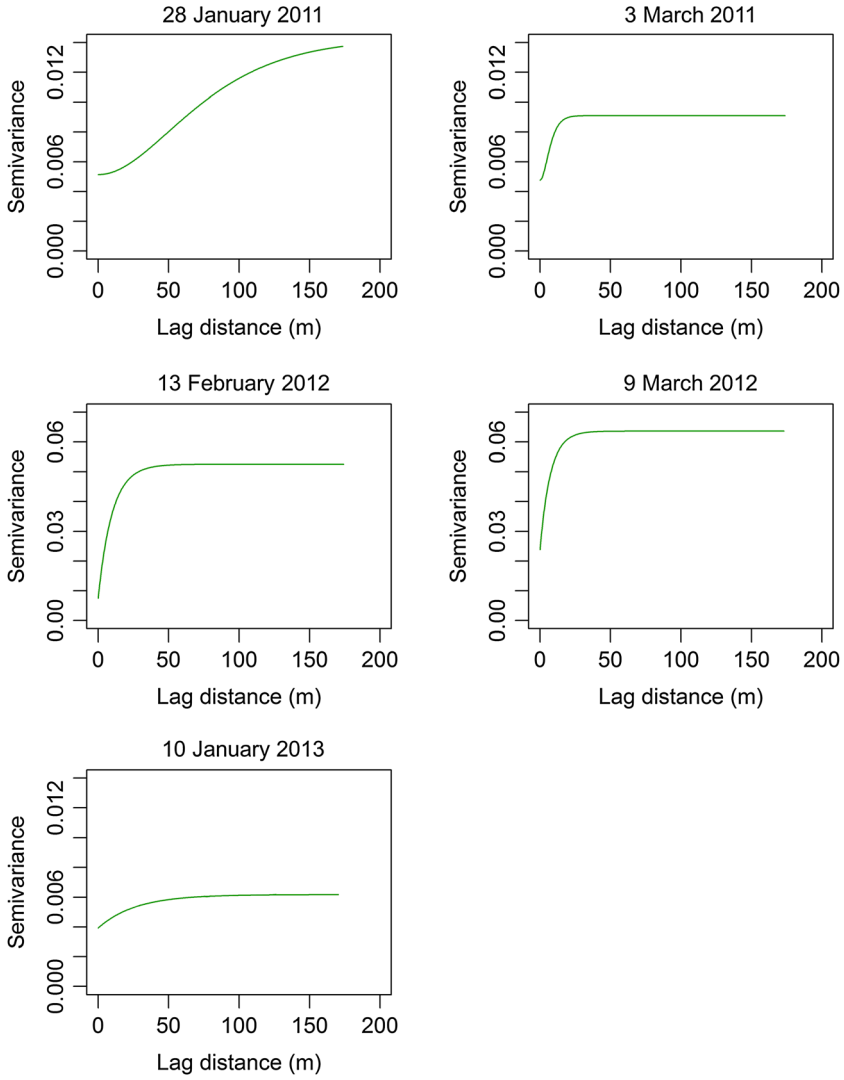

Figure 5. Covariance models of the modeled critical crack length for all five field campaigns estimated with the restricted maximum likelihood method.

Table 2. Measured and Predicted Values With Mean and Standard Deviation (SD) of the Two Instability Criteria S and r_c for the Measurement Locations on the Five Field Days[a]

	Criterion	Measurement (Mean ± SD)	Prediction (Mean ± SD)	Prediction RMSE	Prediction MAE
28 Jan 2011	S	188 ± 120	173 ± 82	93	58
28 Jan 2011	r_c	(38 ± 10) cm	(38 ± 7) cm	9 cm	6 cm
3 Mar 2011	S	167 ± 145	149 ± 62	140	67
3 Mar 2011	r_c	(26 ± 9) cm	(26 ± 5) cm	10 cm	7 cm
13 Feb 2012	S	207 ± 208	194 ± 179	127	76
13 Feb 2012	r_c	(46 ± 15) cm	(45 ± 10) cm	10 cm	7 cm
9 Mar 2012	S	231 ± 165	226 ± 163	141	90
9 Mar 2012	r_c	(46 ± 15) cm	(46 ± 10) cm	13 cm	10 cm
10 Jan 2013	S	365 ± 196	340 ± 135	148	114
10 Jan 2013	r_c	(41 ± 8) cm	(41 ± 5) cm	8 cm	6 cm

[a]Prediction errors from tenfold cross validation including root-mean-square error (RMSE) and mean absolute error (MAE).

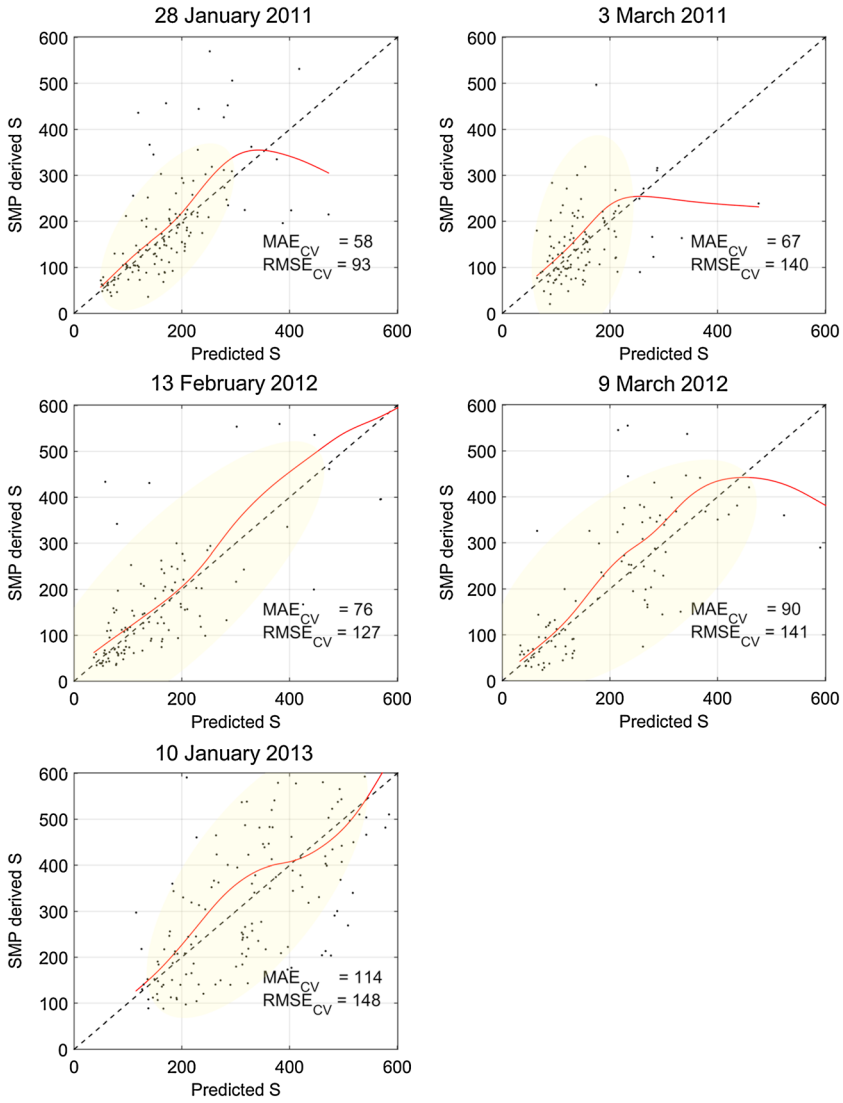

Figure 6. Comparisons of SMP-derived and SMP-predicted failure initiation criterion *S* from cross validation (CV) (dots) with smoothing spline in red and 1:1 line in black (dashed) for all five field campaigns. Yellow bulb covers 1 standard deviation of the data.

3.3. Spatial Prediction

Based on the external drift model and the autocorrelation structure identified for both snow instability criteria, we calculated spatial predictions for both snow instability criteria and analyzed the prediction errors to assess the uncertainty involved with the mapping.

The results of the external drift kriging predictions and their errors are summarized in Table 2. The average predicted values of the failure initiation criterion were within 10% of the SMP-derived values at the measurement locations. They were all considerably larger than the errors for the critical crack length. On all days, the average predicted values of the critical crack lengths at the measurements locations were within ±1 cm of the SMP-derived critical crack lengths.

SMP-derived values and values predicted with tenfold cross validation of the failure initiation criterion and the critical crack length are contrasted in scatterplots in Figures 6 and 7, respectively. The smoothing spline is close to the 1:1 line in the plots where the point density is high. Deviations from the 1:1 line were largest in case of the failure initiation criterion on 9 March 2012 and 10 January 2013 (Figure 6), which is reflected in the highest mean absolute errors (MAE = 90 and MAE = 114, respectively) of the predicted failure initiation

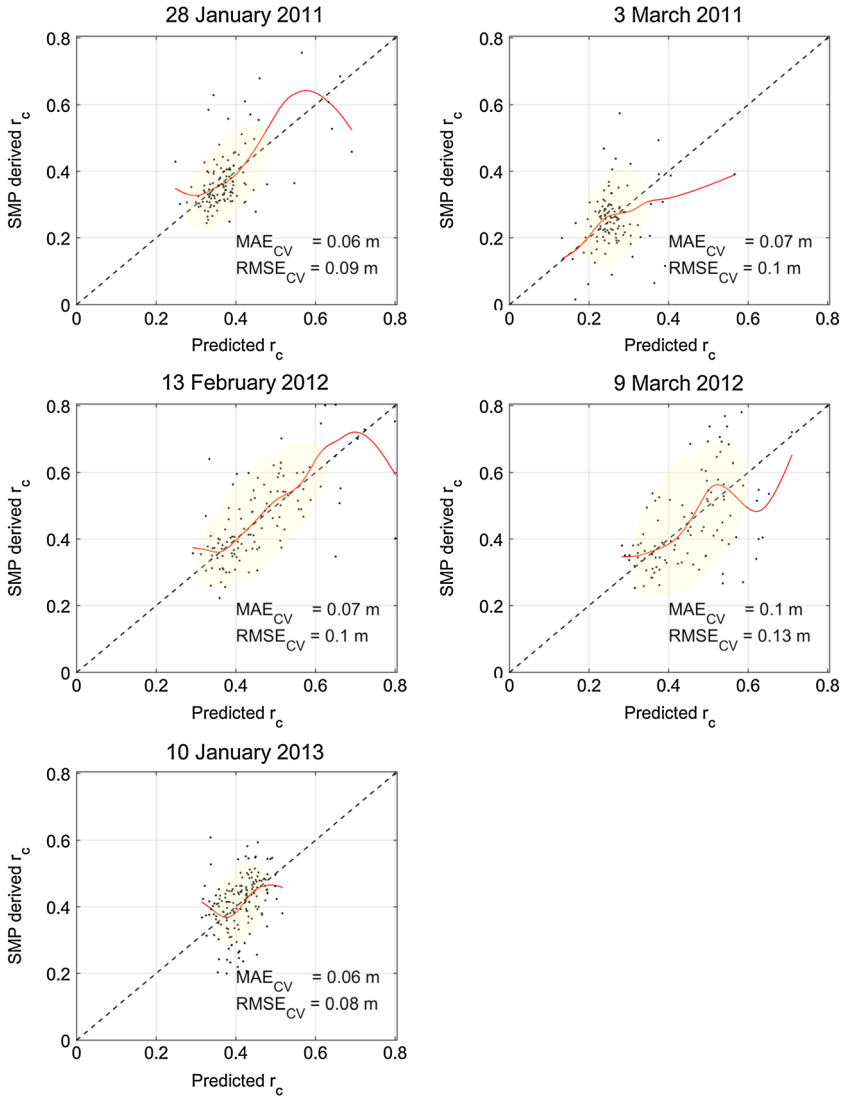

Figure 7. Comparisons of SMP-derived and SMP-predicted critical crack length r_c (m) from cross validation (CV) (dots) with smoothing spline in red and 1:1 line in black (dashed) for all five field campaigns. Yellow bulb covers 1 standard deviation of the data.

criterion on the two days (Table 2). For the critical crack length, the deviation of the smoothing spline from the 1:1 line was less pronounced (Figure 7), with the largest mean absolute error on 9 March 2012 (MAE = 10 cm). Plots for SMP-derived and SMP-predicted critical crack length showed few scatter (Figure 7), except on 9 March 2012, which is in line with low root-mean-square prediction errors only slightly larger than the SMP-derived critical crack length modeling error, namely, root-mean-square error (RMSE = 7 cm) and mean absolute error (MAE = 2 cm) as reported by *Reuter et al.* [2015a]. The smallest error (RMSE = 8 cm) was obtained on 10 January 2013, when the autocorrelation was modeled with the highest restricted log likelihood (Table 1).

Summing up, predictions of the failure initiation criterion were less reliable compared to the spatial predictions of the critical crack length. While with the external drift model a larger amount of variation of the failure initiation criterion was captured than in case of the critical crack length, the residuals of the failure initiation criterion were less clearly autocorrelated and the fits of the covariance model performed less well according to the values of restricted log likelihood in Table 1. The lower level of residual autocorrelation is one reason for the less reliable predictions for the failure initiation criterion apart from an inherently higher variance in the failure initiation criterion indicated by the scatter in Figure 6.

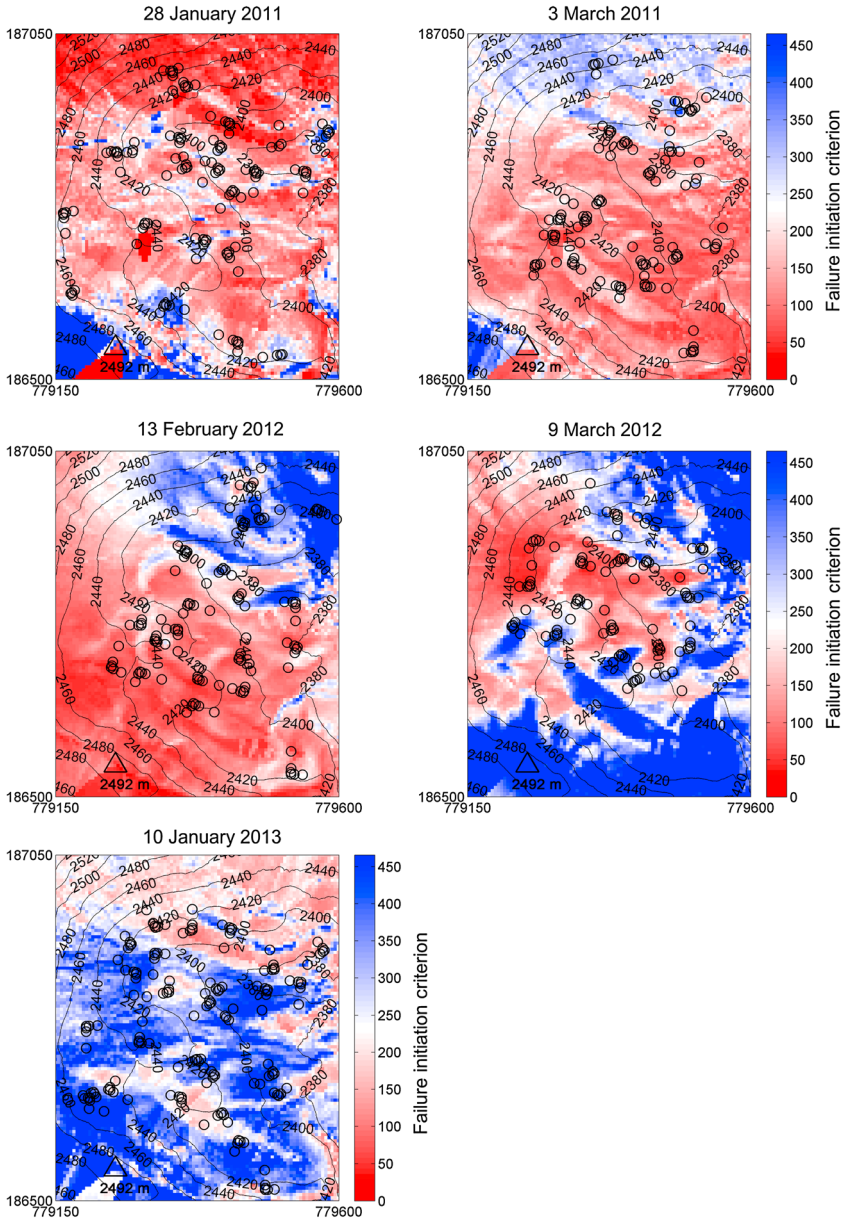

Figure 8. Maps of the failure initiation criterion predicted with external drift kriging for all five field campaigns for the Steintälli field site. Axes are labeled with Swiss coordinates (in meters). Triangle indicates an AWS at an elevated point on the ridge.

Furthermore, Figures 6 and 7 illustrate the nonspatial distribution of modeled snow instability criteria at the measurement locations which is highlighted by a bulb around the mean with 1 standard deviation. For example, on 13 February 2012 the propensity of failure initiation was generally high as the point cloud is located in the lower left and most values are below the threshold of 234 reported by *Reuter et al.* [2015a]. However, the scatter was large indicated by the large size of the bulb. In contrast, the propensity for crack propagation was not very pronounced due to generally intermediate to high values of the critical crack length (0.4-0.6 m) according to the threshold of 0.41 m reported by *Reuter et al.* [2015a].

To visualize the spatial distribution of snow instability, the prediction was carried out across the entire Steintälli basin. The results were mapped and are presented in Figures 8 and 9. Blue colors indicate values above the thresholds reported by *Reuter et al.* [2015a], i.e., high values of snow stability, red colors indicate

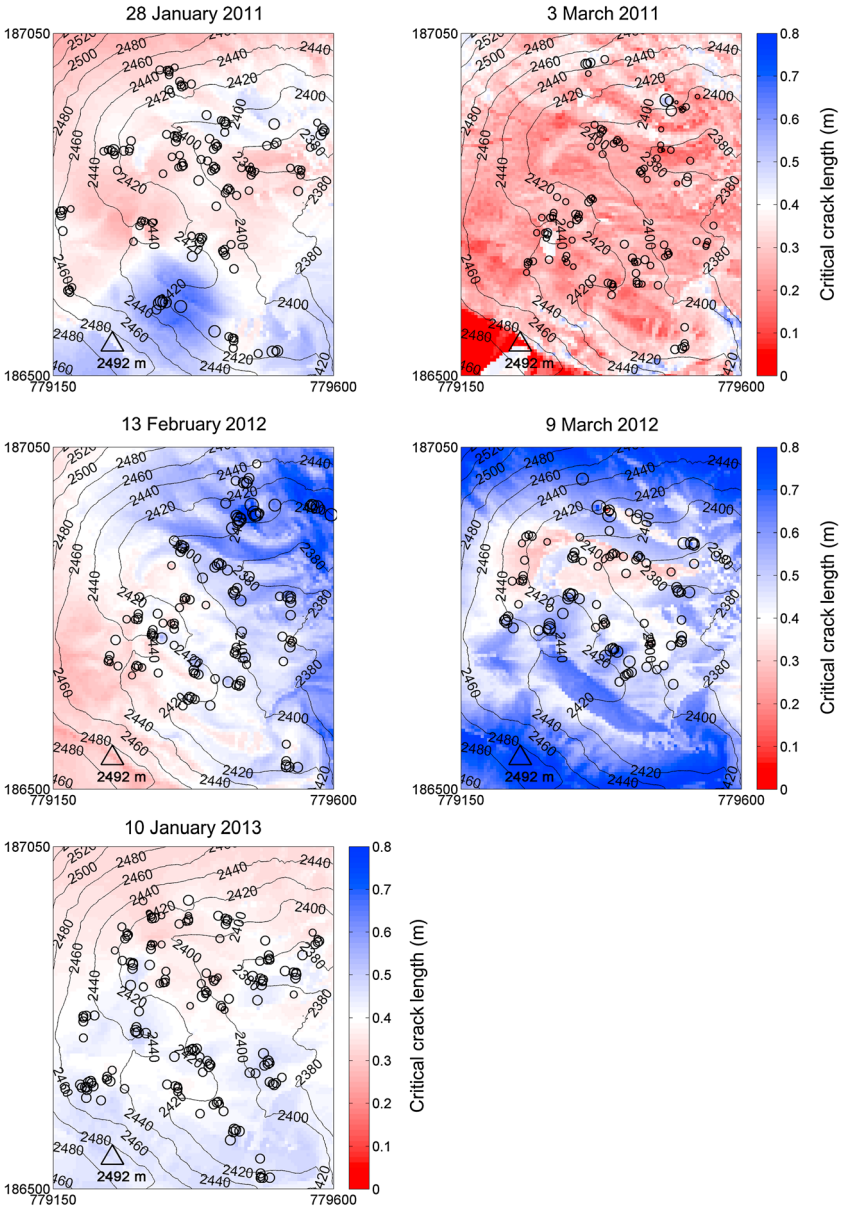

Figure 9. Maps of the critical cut length predicted with external drift kriging for all five field campaigns for the Steintälli field site. Axes are labeled with Swiss coordinates (in meters). Triangle indicates an AWS at an elevated point on the ridge.

values below these thresholds, i.e., low values of snow stability. As shown above snow instability variations were partly explained by snow depth and terrain parameters (Table 1). Apparently, snow instability patterns followed terrain features, i.e., areas with similar values of snow instability were found in areas with similar topography, which is reflected in Figures 8 and 9. For instance, on 28 January 2011, when slope angle and aspect were both covariates, a flat area slightly northeast and a rather flat area near the AWS in the center of the sampling area (Figure 1) had lower values of the critical crack length compared with the rest of the sampling domain (Figure 9). In view of the crack propagation propensity on all days except on 3 March 2011 intermediate to high values of the critical crack length were modeled (Figure 9). On 3 March 2011 lower critical crack lengths were predicted in the center of the basin than in the north on the south facing slopes. With regard to failure initiation that pattern, meaning lower values in the center of the basin than on the south facing slopes, was observed more frequently, namely, on 3 March 2011, 13 February 2012, and 9 March 2012 (Figure 8). On the other two days the pattern was reversed with lower values of the failure initiation criterion on the south facing slopes in the north of the basin. Moreover, 3 March 2011 was the only day

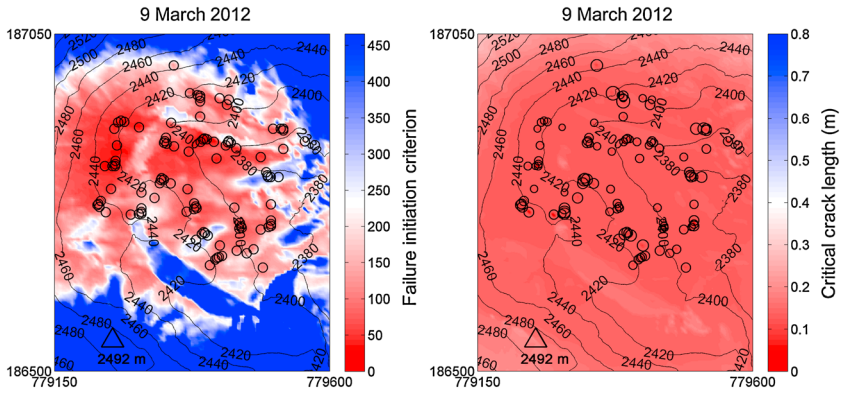

Figure 10. (left) Selected maps presenting the standard prediction error of the failure initiation criterion and (right) the critical crack length for 9 March 2012. Axes are labeled with Swiss coordinates (in meters). Triangle indicates an AWS at an elevated point on the ridge.

with both snow instability criteria yielding below threshold values in most of the sampling area (red colors in Figures 8 and 9). In fact, that day the avalanche danger level was highest among all field campaigns and verified to have been "considerable." On the other sampling days the avalanche danger level was lower, i.e., "low" or "moderate."

The uncertainty of the interpolation of the snow instability criteria at the field site is presented in Figure 10 for 9 March 2012 by the root-mean-square prediction errors. It is obvious that prediction errors of the critical crack length are smaller within the entire sampling area and slightly beyond, whereas the uncertainty of the predicted failure initiation criterion increases quickly away from sampled locations. In the case of the failure initiation criterion, variations depend more strongly on terrain, than on the autocorrelation structure compared to the critical crack length, as presented in sections 3.1 and 3.2. Hence, varying the terrain, which is equivalent to moving away from sampling locations, increases the prediction uncertainty more rapidly in the case of the failure initiation criterion.

3.4. Identifying Causes of Snow Instability Variations

Aiming at identifying meteorological drivers, we built the geostatistical model (section 2.5.1) on snow cover covariate data, which were modeled from meteorological input with Alpine3D. For one specific case, 3 March 2011, we made an initial attempt to identify the drivers of snow instability variations by tracking back the meteorological conditions. To this end, we repeated the geostatistical analysis and we had performed hitherto, with snow cover related covariates instead of terrain parameters and snow depth. As the covariates we selected the first two components of a principle component analysis applied to the SNOWPACK output variables: weak layer shear strength, shear stress at the depth of the weak layer, load of the slab, average density of the slab, slab thickness, and the skier stability index.

For both snow instability criteria, the load due to the weight of the slab and the shear stress at the depth of the weak layer described the snow instability variations in the basin. Both parameters are based on slope angle, density, and the thickness of the slab. The regression model was significantly better than a regression based on topographic coordinates only (Akaike information criterion). The covariance models fitting the variograms best indicated a smooth surface (corresponding to Matérn with $\eta = 2.5$), and the range was derived to 5 m for S and 7 m for r_c (Table 3). From tenfold cross validation we obtained similar prediction errors as with

Table 3. Results of the Geostatistical Analyses Based on Snow Cover Modeling-Derived Covariates[a]

	Criterion	Covariates	Log	R_a^2	Covariance Function	Range
3 Mar 2011	S	Load + weak layer shear stress	Yes	0.18	Matérn with $\eta = 2.5$	5 m
3 Mar 2011	r_c	Load + weak layer shear stress	No	0.06	Matérn with $\eta = 2.5$	7 m

[a]For 3 March 2011 for both response variables S and r_c the variables included in the PCA components (covariates) are presented. Furthermore, the information whether the response variable was log transformed (yes/no), the adjusted coefficient of determination (R_a^2) of the regression model and the range estimated from the covariance model are given.

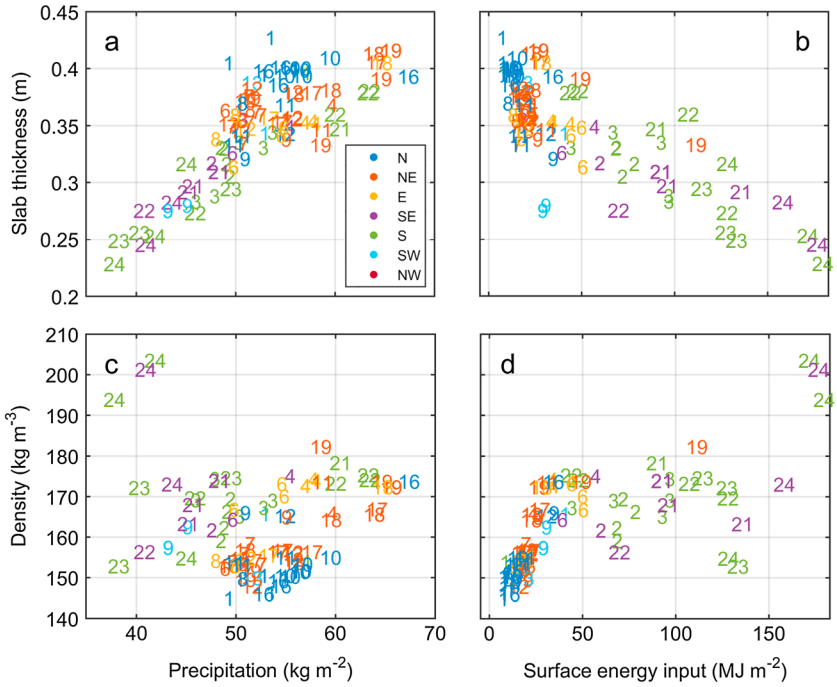

Figure 11. Slab thickness and average slab density versus sum of precipitation and sum of energy fluxes at the snow surface during the slab formation period. All values obtained from snow cover modeling. Colors indicate aspect, and the numbers refer to the grid cells presented with the sampling design in Figure 1.

the terrain-based statistical model (RMSE = 143 for the failure initiation criterion and RMSE = 10 cm for the critical crack length) (cf. Table 2).

For the obtained snow instability variations on 3 March 2011, we were finally searching for the meteorological drivers that had caused the variations of slab load and weak layer stress. These two slab properties mostly depend on snow density and slab thickness. The meteorological variables were integrated over the slab formation period between 24 January and 3 March 2011, as both slab density and thickness are slab parameters. A linear regression analysis indicates that the slab thickness was related to the total sum of precipitation ($R^2 = 0.64$) (Figure 11a) and the total energy input at the snow surface ($R^2 = 0.58$) during the slab formation period (Figure 11b) at the sampling locations. The average density of the slab was rather driven by the energy input at the snow surface ($R^2 = 0.52$) (Figure 11d) than by the total sum of precipitation ($R^2 < 0.01$) during the slab formation period (Figure 11c).

With smaller amounts of precipitation and higher energy inputs at the same time thinner slabs had developed in the south and southeast facing slopes in the northern part of the sampling area resulting in a lower propensity for crack propagation on these slopes (Figure 9). In this area, also the propensity for failure initiation was lowest. The relatively long critical crack lengths on the slopes of northern aspect, e.g., in the southernmost grid cell (Figure 9), can also be explained with lower slab densities caused by a significantly lower energy input due to the aspect-related differences in radiation (Figure 11d).

Interestingly, the skier stability index SK_{38} was not included into principal component analysis (PCA) since it was slightly negatively correlated ($R^2 = 0.05$) with our failure initiation criterion S—although they are based on the same parameters. Furthermore, SK_{38} modeled with SNOWPACK was previously validated and found to be related to observed snow instability [*Schweizer et al.*, 2006]. To find the reason for this discrepancy, we contrasted the key model parameters with the measured opponents.

In Figure 12a we compare average slab densities as measured with the SMP and modeled with Alpine3D. The variations produced by the snow cover model ranged from 145 to 200 kg m^{-3} and considerably underestimated the variations measured with the SMP (145-390 kg m^{-3}) (Figure 12a). Furthermore, the modeled variations in snow depth were much less prominent than actually observed with the TLS measurements—though

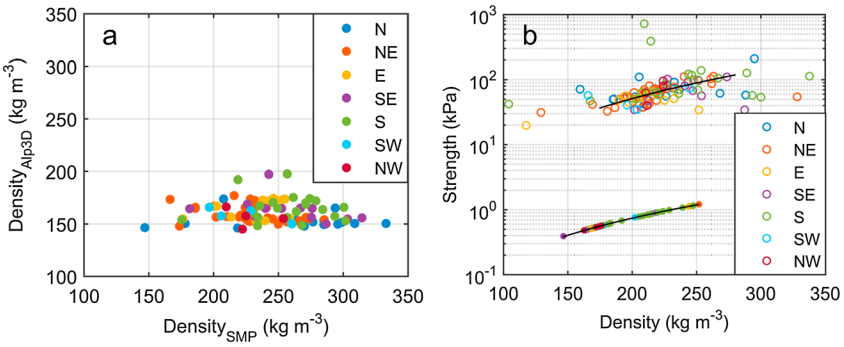

Figure 12. (a) Comparison of average slab density obtained from SMP measurements and from Alpine3D snow cover modeling for all sampling locations; colors indicate aspect. (b) Shear strength versus density of the weak layer as obtained from Alpine3D snow cover simulations (full circles). Compressive strength versus density of the weak layer as measured with the SMP (open circles); black lines are power law fits; colors indicate aspect. ($N = 110$, one outlier not shown.)

the average snow depths agreed well (Alpine3D: 1.37 m and TLS: 1.44 m). The less prominent snow depth variations may have contributed to the low variation in modeled snow density.

In Figure 12b we contrast modeled shear strength and SMP-derived strength. Note the SMP-derived values are about two orders of magnitude higher, because SMP-derived strength rather refers to the compression than to the shear mode and values are not calibrated. In the snow cover module the calculation of the shear strength of persistent weak layers is based on snow density ρ:

$$\tau_s = a\left(\frac{\rho}{\rho_{\text{ice}}}\right)^b \tag{7}$$

with $a = 18.5$ kPa and $b = 2.11$, and ρ_{ice} the density of ice [*Jamieson and Johnston*, 2001]. Performing a robust linear regression of the SMP-derived strength for the part of snow density data containing many measurements (175–280 kg m^{-3}) yielded a coefficient $a = 2.3$ MPa and an exponent $b = 2.49$. The similar exponents indicate that the increase of SMP-derived strength with density is in line with the shear frame measurements by *Jamieson and Johnston* [2001]. The modeled values of shear strength, however, showed little variation since the parameterization is primarily based on snow density which was underestimated by the model.

In summary, the overall low variation in density seems to be responsible for the lack of correlation between the modeled skier stability index and our initiation criterion.

4. Discussion

A geostatistical approach to predict snow instability at the basin scale was applied to snow property data from five field campaigns collected with the snow micropenetrometer in a small basin above tree line. The data were recently presented by *Reuter et al.* [2015b] who performed a first nonspatial analysis to explore potential drivers, mainly terrain and snow depth. Building on their work, the current study aims at describing the spatial variations of snow instability at the basin scale and finally at identifying the causes. To this end, a robust maximum likelihood estimation technique was applied to determine the coefficients of an external drift model and evaluate the spatial autocorrelation structure, which were both used to eventually predict snow instability from point measurements.

4.1. External Drift Model

Terrain is a prominent driver of snow instability at the basin scale and with slope aspect; in particular, observed variations of snow instability were partly explained on all sampling days. This finding agrees well with previous studies at scales beyond the slope scale [*Birkeland*, 2001; *Schweizer and Kronholm*, 2007; *Schweizer et al.*, 2003b]. Similarly, it has been shown that terrain is the most important driver for snow depth [e.g., *Schirmer et al.*, 2011]—which is to some extent related to snow instability [*Reuter et al.*, 2015b; *Schweizer et al.*, 2003b].

For every situation the best fitting model for the available driving agents was chosen by stepwise regression to only include significant driving agents in the models, by the Akaike information criterion to compromise between overfitting and information gain. The regression models varied compared to the previous study by *Reuter et al*. [2015b] as we had to log transform the response variable in some cases (Table 1) to make sure the assumption of weak stationarity was fulfilled for further geostatistical analysis and also as we included topographic coordinates. Prior to the analysis, it was not clear which set of covariates controlled the distribution of snow instability, and the covariates had to be chosen for each situation separately. Although aspect was always among the significant covariates, its influence on snow instability variations varied, for example, north facing slopes may be more stable than south facing slopes (10 January 2013) or vice versa (13 February 2012) (Figures 8 and 9). The lack of a general rule characterizing the distribution of snow instability at all times agrees with our picture of snow instability varying in time and space [*McClung and Schweizer*, 1999]. Meteorological processes vary in time, interact with terrain, and thus cause spatially and temporally varying snow physical properties.

4.2. Spatial Autocorrelation

Our snow instability criteria include several snow physical properties and hence comprise processes on different temporal and spatial scales [*Schweizer and Kronholm*, 2007]. The chosen geostatistical approach divides variations of snow instability into a background field consisting of terrain parameters or snow depth representing a constant or seasonal average and residual patterns partly due to meteorological forcing. With our sampling design having an extent of about 500 m we identified autocorrelation ranges between 5 and 26 m, except for one case of 68 m. These values are similar to the ranges for instability-related parameters determined at the slope scale in previous studies: $r_a = 2–8$ m at an extent of 19 m [*Bellaire and Schweizer*, 2011], $r_a = 2–8$ m at an extent of 19 m [*Schweizer and Reuter*, 2015], and $r_a = 1\text{-}13$ m at extents of 23 and 37 m [*Lutz et al*., 2007]. Obviously, ranges determined previously—though in some cases half the extent—were meaningful, as typical ranges found in the present study at an extent of 500 m were not considerably larger. Comparing with the terrain, obtained ranges were typically shorter than the autocorrelation range of the terrain in the Steintälli area, which has values between 47 and 102 m depending on direction. As snow instability variations due to terrain were modeled with the external drift model and autocorrelation ranges are shorter than the scale on which terrain varies, obtained autocorrelation ranges are suggested to be due to micrometeorological processes causing slope scale variations. The smoothness of the variations modeled by the shape parameter of the fitted covariance model varied between the field days but was always the same for both instability criteria—reflecting the small-scale variability at the particular sampling day. However, strong stability variations below 3 m have not frequently been observed. *Birkeland et al*. [2010] revisited 25 studies in search for an optimal distance for stability test spacing and found only in 2 out of 25 studies strong snow instability variations below 5 m.

4.3. Spatial Prediction

For all sampling days, we performed external drift kriging predictions from multiple regressions based on terrain and snow depth data and the remaining residual autocorrelation. Typically, uncertainties—determined with 10-fold cross validation—were larger for the failure initiation criterion than for the critical crack length. According to higher adjusted R_a^2 the external drift model explained more variation of the failure initiation criterion than of the critical crack length. However, the residuals of the critical crack length were more clearly autocorrelated as reflected in higher values of the restricted log likelihood which yielded a better prediction performance in the end. Also, possibly due to inherently more scattering of the failure initiation criterion itself compared with the critical crack length, the prediction did not reach the same performance. The cross validation prediction errors yielded similar values as the root-mean-square error of 7 cm of the method to derive the critical crack length from an SMP signal [*Reuter et al*., 2015a]. Hence, snow instability may be mapped reliably based on our data.

After first maps had been presented for snow instability-related indices at the slope scale [*Bellaire*, 2010; *Kronholm and Schweizer*, 2003; *Schweizer et al*., 2008b; *Schweizer and Reuter*, 2015], we presented detailed maps of snow instability variations based on field measurements and external drift kriging predictions at the basin scale. Supporting earlier studies based on snow stability observations, [*Birkeland*, 2001; *Schweizer et al*., 2003b] our maps showed that variations of snow instability followed terrain features. The maps may be interpreted according to the sequence of avalanche release processes in the sense that if failure initiation

is likely the crack propagation propensity has to be considered, highlighting the importance of both processes to promote snow instability [*Schweizer et al*., 2003a]. However, at increasing distances from the sampling locations interpretation requires more caution in particular for maps of the failure initiation criterion.

4.4. Causes of Snow Instability Variations

Proxy data for snow instability estimation typically include meteorological data [*Perla*, 1970], but the predictive power is limited if concluding from meteorological data on avalanche hazard [*Schweizer and Föhn*, 1996]. The approach of predicting snow instability variations from meteorological data is basically hampered by the temporal and spatial variations of the snow cover and the missing interaction with terrain. For example, *Schirmer et al*. [2009] made an attempt to include spatial variations in their forecasting model by considering the SNOWPACK output for two rather than one AWS and corresponding virtual slope simulations, but the prediction performance did not improve—suggesting that the modeled variation was not sufficiently meaningful.

To consider the temporal influence of the meteorological forcing and the spatial interactions of meteorological processes with terrain, we repeated the geostatistical analysis with covariates of snow cover data modeled with Alpine3D for the field campaign of 3 March 2011. If the spatial predictions of the failure initiation criterion and the critical crack length were based on snow cover model rather than terrain and snow depth data, the same autocorrelation ranges, the same type of autocorrelation representing a rather smooth surface, and similar cross-validation model errors were obtained. These results suggest that 3-D snow cover modeling with Alpine3D is able to mimic variations of snow properties due to meteorological forcing interacting with terrain—but not variations of snow instability. However, this might be feasible as *Mott et al*. [2011a] have shown for snow ablation which depends on similarly complex micrometeorological processes.

To identify the meteorological processes which shaped the observed variations of snow instability, we analyzed meteorological variables. Preferential deposition of precipitation and differences in the energy input at the snow surface controlled the thickness and the density of the slab. The differences in snow instability (Figure 9) were eventually explained with variations in total amount of precipitation or the energy input at the snow surface during the formation period of the slab (Figure 11). In agreement with *Kozak et al*. [2003], who was able to relate snow layer hardness to snow and air temperature indices or radiation, variations of snow density were related to the energy input at the snow surface and influenced snow instability. Also, relations of the total amount of precipitation with slab thickness and density were plausible and intuitive, so we are confident that precipitation and energy input at the snow surface were mainly responsible for the variations of instability we found on this particular sampling day.

Comparing the snow cover model output with our measurements, we found that the variations of snow density, snow strength, and snow depth modeled with Alpine3D were smaller than measured with the SMP or TLS. The findings suggest that the model is able to mimic snow property variations but does not cover all processes leading to variations of snow instability nor fully capture their influence. We anticipate an improvement in snow cover model performance, once a full description of short and longwave reflections [*Helbig et al*., 2010] and an atmospheric flow field to account for all snow transport processes are considered [*Mott et al*., 2011b]. Moreover, the comparison of SMP-derived snow strength with the shear strength parametrization of *Jamieson and Johnston* [2001] supports previous findings that the snow micropenetrometer is a reliable field measurement tool to acquire snow properties [*Marshall and Johnson*, 2009; *Proksch et al*., 2015; *Reuter et al*., 2015a; *van Herwijnen et al*., 2009].

5. Conclusions

We derived two snow instability criteria from stratified snow micropenetrometer measurements within a basin and performed robust geostatistical analyses for five sampling days with the aim to describe spatial patterns and identify their causes. Using external drift kriging, we interpolated the snow instability measures at the basin scale and provide first exemplary maps.

The external drift model was based on terrain and snow depth, i.e., a constant or seasonal average, respectively. Significant covariates, among which slope aspect was the most prominent, varied depending on the situation. In other words, there is no general rule how terrain parameters relate to snow instability. The sets of covariates explained more variation of the failure initiation criterion than of the critical crack length. In contrast, the residual patterns of the critical crack length were more clearly autocorrelated than in the case

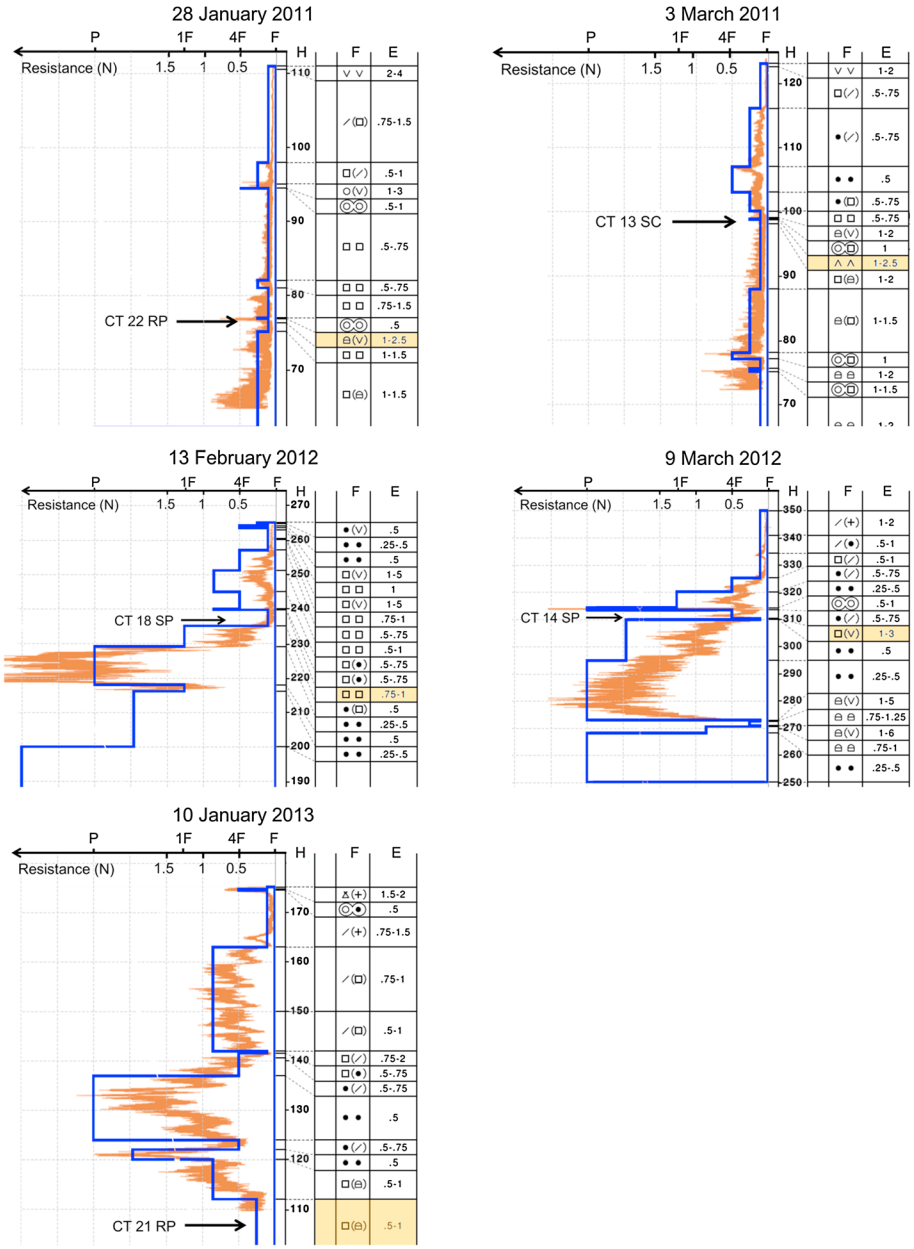

Figure A1. SMP profiles (orange) recorded at the corner point of grid cell 9 for each field day overlain by traditional snow profile data including hand hardness index (blue), snow depth *H* (cm), grain type *F*, and grain size *E* (mm). Critical weakness highlighted in orange and characterized by the compression test (CT) result: CT score and fracture type.

of the failure initiation criterion. For this reason and possibly due to less scatter of the SMP-derived critical crack length, its spatial prediction was more reliable. The resulting maps clearly showed how the propensity for failure initiation and crack propagation varied in our study site depending on terrain. Only when both snow instability criteria yielded below threshold values in most of the sampling area, the avalanche danger rating was considerable indicating critical conditions. For both criteria we modeled rather short autocorrelation ranges (5-31 m and once 68 m) similar to the ranges found in previous slope scale studies and clearly below the autocorrelation ranges of the terrain. We conclude that previously determined ranges at the slope scale were meaningful, despite short extents in sampling designs. Snow instability variations due to terrain were captured with the external drift model, and autocorrelation ranges were shorter than those of the terrain. This finding suggests the autocorrelated variations were due to micrometeorological processes causing variations at the slope scale.

For one situation we identified the meteorological forcing responsible for the observed snow instability variations at the basin scale. Repeating the geostatistical analysis with modeled snow cover data as covariates, we obtained the same autocorrelation ranges and similar prediction errors for both instability criteria. This approach allowed us for the first time to track back potential causes for the variations of snow instability. The observed variations were mainly due to variations in slab layer properties which in the case of 3 March 2011 were caused by preferential deposition of precipitation and energy input at the snow surface during the formation period of the slab layers.

Our results demonstrate the value of 3-D snow cover modeling for enhancing snow instability predictions. Despite this benefit, comparisons with field measurements showed that with our model setup the variations of snow cover properties such as density, snow depth, and snow strength were underestimated. This shortcoming calls for more advanced snow cover modeling to better resolve micrometeorological spatial interactions which are required to capture realistic variations of snow cover properties. In order to fully exploit the potential of snow cover modeling for snow instability prediction, all possible meteorological spatial interactions should be considered in future work. Furthermore, the spatial variability data can be used for realistic simulations with slope failure models.

Appendix A

Snow profile data including the corresponding SMP signal are presented in Figure A1 for each sampling day. The profiles were recorded in a flat area close to the weather station in grid cell 9 and represent the characteristic snow layering observed in the field site.

Acknowledgments
We acknowledge the constructive comments by two anonymous reviewers. We would like to thank Andreas Papritz for the advice on the geostatistical analyses, Jochen Veitinger for the support with TLS data processing, Mathias Bavay for the help with the Alpine3D model setup, Rebecca Mott and Michael Lehning for commenting on the manuscript. Moreover, we are grateful to all colleagues involved in the field campaigns, in particular Thomas Grünewald, Anna Haberkorn, Christoph Mitterer, Lino Schmid, Stephan Simioni, and Walter Steinkogler. B.R. has been supported by a grant of the Swiss National Science Foundation (200021_144392). The presented data are available on request.

References

Anderson, T. L. (2005), *Fracture Mechanics: Fundamentals and Applications*, 3rd ed., 640 pp., CRC Press, Boca Raton, Fla.
Bavay, M., and T. Egger (2014), MeteoIO 2.4.2: A preprocessing library for meteorological data, *Geosci. Model Dev.*, *7*(6), 3135–3151, doi:10.5194/gmd-7-3135-2014.
Bellaire, S. (2010), Spatial variability of the snow cover and its effect on avalanche formation, PhD thesis, 196 pp, Univ. of Hamburg, Hamburg, Germany.
Bellaire, S., C. Pielmeier, M. Schneebeli, and J. Schweizer (2009), Stability algorithm for snow micro-penetrometer measurements, *J. Glaciol.*, *55*(193), 805–813.
Bellaire, S., and J. Schweizer (2011), Measuring spatial variations of weak layer and slab properties with regard to snow slope stability, *Cold Reg. Sci. Technol.*, *65*(2), 234–241, doi:10.1016/j.coldregions.2010.08.013.
Birkeland, K., K. Kronholm, M. Schneebeli, and C. Pielmeier (2004a), Changes in shear strength and micropenetration hardness of a buried surface-hoar layer, *Ann. Glaciol.*, *38*, 223–228.
Birkeland, K., S. Logan, and K. Kronholm (2004b), A comparison of the spatial structure of the penetration resistance of snow layers in two different snow climates, in *Proceedings ISSMA-2004. International Symposium on Snow Monitoring and Avalanches*, pp. 3–11, Snow and Avalanche Study Establ., Manali, India.
Birkeland, K. W. (2001), Spatial patterns of snow stability throughout a small mountain range, *J. Glaciol.*, *47*(157), 176–186.
Birkeland, K. W., J. Hendrikx, and M. P. Clark (2010), On optimal stability-test spacing for assessing snow avalanche conditions, *J. Glaciol.*, *56*(199), 795–804, doi:10.3189/002214310794457281.
Birkeland, K. W., K. Kronholm, S. Logan, and J. Schweizer (2006), Field measurements of sintering after fracture of snowpack weak layers, *Geophys. Res. Lett.*, *33*, L03501, doi:10.1029/2005GL025104.
Blöschl, G., and M. Sivapalan (1995), Scale issues in hydrological modelling—A review, *Hydrol. Process.*, *9*, 251–290.
Bühler, Y., M. Marty, and C. Ginzler (2012), High resolution DEM generation in high-Alpine terrain using airborne remote sensing techniques, *Trans. GIS*, *16*(5), 635–647, doi:10.1111/j.1467-9671.2012.01331.x.
Campbell, C., and J. B. Jamieson (2007), Spatial variability of slab stability and fracture characteristics within avalanche start zones, *Cold Reg. Sci. Technol.*, *47*(1–2), 134–147.
Conway, H., and J. Abrahamson (1984), Snow stability index, *J. Glaciol.*, *30*(106), 321–327.
Conway, H., and J. Abrahamson (1988), Snow-slope stability—A probabilistic approach, *J. Glaciol.*, *34*(117), 170–177.
Diggle, P. J., and P. J. Ribeiro (2007), *Model-Based Geostatistics*, pp. 232, Springer, New York, doi:10.1007/978-0-387-48536-2.
Draper, N. R., and H. Smith (1998), *Applied Regression Analysis*, 3rd ed., John Wiley, New York.
Elder, K., D. Cline, G. E. Liston, and R. Armstrong (2009), NASA Cold Land Processes Experiment (CLPX 2002/03): Field measurements of snowpack properties and soil moisture, *J. Hydrometeorol.*, *10*(1), 320–329, doi:10.1175/2008jhm877.1.
Erbs, D. G., S. A. Klein, and J. A. Duffie (1982), Estimation of the diffuse radiation fraction for hourly, daily and monthly-average global radiation, *Sol. Energy*, *28*(4), 293–302, doi:10.1016/0038-092X(82)90302-4.
Fierz, C., R. L. Armstrong, Y. Durand, P. Etchevers, E. Greene, D. M. McClung, K. Nishimura, P. K. Satyawali, and S. A. Sokratov (2009), *The International Classification for Seasonal Snow on the Ground*, pp. 90, UNESCO-IHP, Paris, France.
Föhn, P. M. B. (1989), Snow cover stability tests and the areal variability of snow strength, in *Proceedings International Snow Science Workshop, Whistler, British Columbia, Canada, 12–15 October 1988*, edited, pp. 262–273, Canadian Avalanche Assoc., Revelstoke BC, Canada.
Frei, C. (2014), Interpolation of temperature in a mountainous region using nonlinear profiles and non-Euclidean distances, *Int. J. Climatol.*, *34*(5), 1585–1605, doi:10.1002/joc.3786.
Fyffe, B., and M. Zaiser (2004), The effects of snow variability on slab avalanche release, *Cold Reg. Sci. Technol.*, *40*(3), 229–242.

Gaume, J., N. Eckert, G. Chambon, M. Naaim, and L. Bel (2013), Mapping extreme snowfalls in the French Alps using max-stable processes, *Water Resour. Res.*, *49*, 1079–1098, doi:10.1002/wrcr.20083.
Gaume, J., J. Schweizer, A. van Herwijnen, G. Chambon, B. Reuter, N. Eckert, and M. Naaim (2014), Evaluation of slope stability with respect to snowpack spatial variability, *J. Geophys. Res. Earth Surf.*, *119*, 1783–1799, doi:10.1002/2014JF00319.
Gaume, J., A. van Herwijnen, G. Chambon, K. W. Birkeland, and J. Schweizer (2015), Modeling of crack propagation in weak snowpack layers using the discrete element method, *Cryosphere*, *9*, 1915–1932, doi:10.5194/tc-9-1915-2015.
Gauthier, D., and B. Jamieson (2008), Evaluation of a prototype field test for fracture and failure propagation propensity in weak snowpack layers, *Cold Reg. Sci. Technol.*, *51*(2–3), 87–97, doi:10.1016/j.coldregions.2007.04.005.
Grünewald, T., M. Schirmer, R. Mott, and M. Lehning (2010), Spatial and temporal variability of snow depth and ablation rates in a small mountain catchment, *Cryosphere*, *4*(2), 215–225, doi:10.5194/tc-4-215-2010.
Haladuick, S., M. Schirmer, and B. Jamieson (2014), What do field observations tell us about avalanche danger?, in *Proceedings ISSW 2014. International Snow Science Workshop, Banff, Alberta, Canada, 29 September - 3 October 2014*, edited by P. Haegeli, pp. 63–66.
Helbig, N., H. Löwe, B. Mayer, and M. Lehning (2010), Explicit validation of a surface shortwave radiation balance model over snow-covered complex terrain, *J. Geophys. Res.*, *115*, D18113, doi:10.1029/2010JD013970.
Hendrikx, J., K. Birkeland, and M. Clark (2009), Assessing changes in the spatial variability of the snowpack fracture propagation propensity over time, *Cold Reg. Sci. Technol.*, *56*(2–3), 152–160.
Jamieson, B., P. Haegeli, and J. Schweizer (2009), Field observations for estimating the local avalanche danger in the Columbia Mountains of Canada, *Cold Reg. Sci. Technol.*, *58*(1–2), 84–91.
Jamieson, J. B., and C. D. Johnston (1993), Rutschblock precision, technique variations and limitations, *J. Glaciol.*, *39*(133), 666–674.
Jamieson, J. B., and C. D. Johnston (1997), The compression test for snow stability, paper presented at Proceedings International Snow Science Workshop, Banff, Alberta, Canada, 6–10 October 1996, Canadian Avalanche Association, Revelstoke BC, Canada.
Jamieson, J. B., and C. D. Johnston (1998), Refinements to the stability index for skier-triggered dry slab avalanches, *Ann. Glaciol.*, *26*, 296–302.
Jamieson, J. B., and C. D. Johnston (2001), Evaluation of the shear frame test for weak snowpack layers, *Ann. Glaciol.*, *32*, 59–68.
Johnson, J. B., and M. Schneebeli (1999), Characterizing the microstructural and micromechanical properties of snow, *Cold Reg. Sci. Technol.*, *30*(1–3), 91–100.
Kozak, M. C., K. Elder, K. Birkeland, and P. Chapman (2003), Variability of snow layer hardness by aspect and prediction using meteorological factors, *Cold Reg. Sci. Technol.*, *37*(3), 357–371.
Kronholm, K. (2004), Spatial variability of snow mechanical properties with regard to avalanche formation, PhD thesis, 192 pp., Univ. of Zurich, Zurich, Switzerland.
Kronholm, K., and K. W. Birkeland (2005), Integrating spatial patterns into a snow avalanche cellular automata model, *Geophys. Res. Lett.*, *32*, L19504, doi:10.1029/2005GL024373.
Kronholm, K., and K. W. Birkeland (2007), Reliability of sampling designs for spatial snow surveys, *Comput. Geosci.*, *33*(9), 1097–1100.
Kronholm, K., M. Schneebeli, and J. Schweizer (2004), Spatial variability of micropenetration resistance in snow layers on a small slope, *Ann. Glaciol.*, *38*, 202–208.
Kronholm, K., and J. Schweizer (2003), Snow stability variation on small slopes, *Cold Reg. Sci. Technol.*, *37*(3), 453–465.
Lehning, M., I. Völksch, D. Gustafsson, T. A. Nguyen, M. Stähli, and M. Zappa (2006), ALPINE3D: A detailed model of mountain surface processes and its application to snow hydrology, *Hydrol. Process.*, *20*(10), 2111–2128, doi:10.1002/hyp.6204.
Liston, G. E., and K. Elder (2006), A meteorological distribution system for high-resolution terrestrial modeling (MicroMet), *J. Hydrometeorol.*, *7*(2), 217–234, doi:10.1175/JHM486.1.
Logan, S., K. W. Birkeland, K. Kronholm, and K. J. Hansen (2007), Temporal changes in the slope-scale spatial variability of the shear strength of buried surface hoar layers, *Cold Reg. Sci. Technol.*, *47*(1–2), 148–158.
Löwe, H., and A. van Herwijnen (2012), A Poisson shot noise model for micro-penetration of snow, *Cold Reg. Sci. Technol.*, *70*, 62–70, doi:10.1016/j.coldregions.2011.09.001.
Lutz, E. R., and K. W. Birkeland (2011), Spatial patterns of surface hoar properties and incoming radiation on an inclined forest opening, *J. Glaciol.*, *57*(202), 355–366.
Lutz, E. R., K. W. Birkeland, K. Kronholm, K. J. Hansen, and R. Aspinall (2007), Surface hoar characteristics derived from a snow micropenetrometer using moving window statistical operations, *Cold Reg. Sci. Technol.*, *47*(1–2), 118–133.
Marshall, H.-P., and J. B. Johnson (2009), Accurate inversion of high-resolution snow penetrometer signals for microstructural and micromechanical properties, *J. Geophys. Res.*, *114*(F4), F04016, doi:10.1029/2009JF001269.
Marty, C., R. Philipona, C. Fröhlich, and A. Ohmura (2002), Altitude dependence of surface radiation fluxes and cloud forcing in the Alps: Results from the alpine surface radiation budget network, *Theor. Appl. Climatol.*, *72*(3–4), 137–155, doi:10.1007/s007040200019.
McClung, D. M., and J. Schweizer (1999), Skier triggering, snow temperatures and the stability index for dry slab avalanche initiation, *J. Glaciol.*, *45*(150), 190–200.
Meister, R. (1995), Country-wide avalanche warning in Switzerland, in *Proceedings International Snow Science Workshop, Snowbird, Utah, U.S.A., 30 October–3 November 1994*, edited, pp. 58–71, ISSW 1994 Organizing Committee, Snowbird Utah.
Mott, R., M., Schirmer, M. Bavay, T. Grünewald, and M. Lehning (2010), Understanding snow-transport processes shaping the mountain snow-cover, *The Cryosphere*, *4*(4), 545–559, doi:10.5194/tc-4-545-2010.
Mott, R., L. Egli, T. Grünewald, N. Dawes, C. Manes, M. Bavay, and M. Lehning (2011a), Micrometeorological processes driving snow ablation in an Alpine catchment, *Cryosphere*, *5*(4), 1083–1098, doi:10.5194/tc-5-1083-2011.
Mott, R., M. Schirmer, and M. Lehning (2011b), Scaling properties of wind and snow depth distribution in an Alpine catchment, *J. Geophys. Res.*, *116*, D06106, doi:10.1029/2010JD014886.
Nussbaum, M., A. Papritz, A. Baltensweiler, and L. Walthert (2014), Estimating soil organic carbon stocks of Swiss forest soils by robust external-drift kriging, *Geosci. Model Dev.*, *7*(3), 1197–1210, doi:10.5194/gmd-7-1197-2014.
Papritz, A. (2013), Georob: Robust geostatistical analysis of spatial data.
Papritz, A., H. R. Künsch, C. Schwierz, and W. A. Stahel (2013), Robust geostatistical analysis of spatial data, *Geophys. Res. Abstr.*, *15*, EGU2012–14,145.
Perčec Tadić, M. (2010), Gridded Croatian climatology for 1961–1990, *Theor. Appl. Climatol.*, *102*(1–2), 87–103, doi:10.1007/s00704-009-0237-3.
Perla, R. (1970), On contributory factors in avalanche hazard evaluation, *Can. Geotech. J.*, *7*, 414–419.
Pielmeier, C., and H.-P. Marshall (2009), Rutschblock-scale snowpack stability derived from multiple quality-controlled SnowMicroPen measurements, *Cold Reg. Sci. Technol.*, *59*(2–3), 178–184.
Pielmeier, C., and J. Schweizer (2007), Snowpack stability information derived from the SnowMicroPen, *Cold Reg. Sci. Technol.*, *47*(1–2), 102–107.

Prokop, A. (2008), Assessing the applicability of terrestrial laser scanning for spatial snow depth measurements, *Cold Reg. Sci. Technol.*, *54*(3), 155–163.
Prokop, A., M. Schirmer, M. Rub, M. Lehning, and M. Stocker (2008), A comparison of measurement methods: Terrestrial laser scanning, tachymetry and snow probing, for the determination of the spatial snow depth distribution on slopes, *Ann. Glaciol.*, *49*, 210–216.
Proksch, M., H. Löwe, and M. Schneebeli (2015), Density, specific surface area and correlation length of snow measured by high-resolution penetrometry, *J. Geophys. Res. Earth Surf.*, *120*, 346–362, doi:10.1002/2014JF003266.
R Core Team (2013), *A Language and Environment for Statistical Computing*, R Foundation for Stat., Computing, Vienna, Austria.
Reuter, B., and J. Schweizer (2012), The effect of surface warming on slab stiffness and the fracture behavior of snow, *Cold Reg. Sci. Technol.*, *83–84*, 30–36, doi:10.1016/j.coldregions.2012.06.001.
Reuter, B., J. Schweizer, and A. van Herwijnen (2015a), A process-based approach to estimate point snow instability, *Cryosphere*, *9*, 837–847, doi:10.5194/tc-9-837-2015.
Reuter, B., A. van Herwijnen, J. Veitinger, and J. Schweizer (2015b), Relating simple drivers to snow instability, *Cold Reg. Sci. Technol.*, *120*, 168–178, doi:10.1016/j.coldregions.2015.06.016.
Schirmer, M., M. Lehning, and J. Schweizer (2009), Statistical forecasting of regional avalanche danger using simulated snow cover data, *J. Glaciol.*, *55*(193), 761–768.
Schirmer, M., V. Wirz, A. Clifton, and M. Lehning (2011), Persistence in intra-annual snow depth distribution: 1. Measurements and topographic control, *Water Resour. Res.*, *47*, W09516, doi:10.1029/2010WR009426.
Schmucki, E., C. Marty, C. Fierz, and M. Lehning (2014), Evaluation of modelled snow depth and snow water equivalent at three contrasting sites in Switzerland using SNOWPACK simulations driven by different meteorological data input, *Cold Reg. Sci. Technol.*, *99*, 27–37, doi:10.1016/j.coldregions.2013.12.004.
Schneebeli, M., C. Pielmeier, and J. B. Johnson (1999), Measuring snow micro structure and hardness using a high resolution penetrometer, *Cold Reg. Sci. Technol.*, *30*(1–3), 101–114.
Schweizer, J., S. Bellaire, C. Fierz, M. Lehning, and C. Pielmeier (2006), Evaluating and improving the stability predictions of the snow cover model SNOWPACK, *Cold Reg. Sci. Technol.*, *46*(1), 52–59.
Schweizer, J., and P. M. B. Föhn (1996), Avalanche forecasting—An expert system approach, *J. Glaciol.*, *42*(141), 318–332.
Schweizer, J., A. Heilig, S. Bellaire, and C. Fierz (2008a), Variations in snow surface properties at the snowpack depth, the slope and the basin scale, *J. Glaciol.*, *54*(188), 846–856.
Schweizer, J., J. B. Jamieson, and M. Schneebeli (2003a), Snow avalanche formation, *Rev. Geophys.*, *41*(4), 1016, doi:10.1029/2002RG000123.
Schweizer, J., and K. Kronholm (2007), Snow cover spatial variability at multiple scales: Characteristics of a layer of buried surface hoar, *Cold Reg. Sci. Technol.*, *47*(3), 207–223, doi:10.1016/j.coldregions.2006.09.002.
Schweizer, J., K. Kronholm, J. B. Jamieson, and K. W. Birkeland (2008b), Review of spatial variability of snowpack properties and its importance for avalanche formation, *Cold Reg. Sci. Technol.*, *51*(2–3), 253–272, doi:10.1016/j.coldregions.2007.04.009.
Schweizer, J., K. Kronholm, and T. Wiesinger (2003b), Verification of regional snowpack stability and avalanche danger, *Cold Reg. Sci. Technol.*, *37*(3), 277–288.
Schweizer, J., and B. Reuter (2015), A new index combining weak layer and slab properties for snow instability prediction, *Nat. Hazards Earth Syst. Sci.*, *15*, 109–118, doi:10.5194/nhess-15-109-2015.
Sigrist, C., and J. Schweizer (2007), Critical energy release rates of weak snowpack layers determined in field experiments, *Geophys. Res. Lett.*, *34*, L03502, doi:10.1029/2006GL028576.
Simenhois, R., and K. W. Birkeland (2009), The Extended Column Test: Test effectiveness, spatial variability, and comparison with the Propagation Saw Test, *Cold Reg. Sci. Technol.*, *59*(2–3), 210–216.
Stössel, F., M. Guala, C. Fierz, C. Manes, and M. Lehning (2010), Micrometeorological and morphological observations of surface hoar dynamics on a mountain snow cover, *Water Resour. Res.*, *46*, W04511, doi:10.1029/2009WR008198.
van Herwijnen, A., S. Bellaire, and J. Schweizer (2009), Comparison of micro-structural snowpack parameters derived from penetration resistance measurements with fracture character observations from compression tests, *Cold Reg. Sci. Technol.*, *59*(2–3), 193–201.
Veitinger, J., B. Sovilla, and R. S. Purves (2014), Influence of snow depth distribution on surface roughness in alpine terrain: A multi-scale approach, *Cryosphere*, *8*(2), 547–569, doi:10.5194/tc-8-547-2014.
Vionnet, V., E. Martin, V. Masson, G. Guyomarc'h, F. Naaim-Bouvet, A. Prokop, Y. Durand, and C. Lac (2014), Simulation of wind-induced snow transport and sublimation in alpine terrain using a fully coupled snowpack/atmosphere model, *Cryosphere*, *8*(2), 395–415, doi:10.5194/tc-8-395-2014.
Webster, R., and M. A. Oliver (2007), *Geostatistics for Environmental Scientists*, 2nd ed., 271 pp., Wiley, Chichester, West Sussex, U. K.
Winstral, A., K. Elder, and R. E. Davis (2002), Spatial snow modeling of wind-redistributed snow using terrain based parameters, *J. Hydrometeorol.*, *3*(5), 524–538.